nature nanotechnology

Article

https://doi.org/10.1038/s41565-026-02247-5

Strain-isolated microneedles for ambulatory hormonal and metabolic monitoring

Received: 28 January 2026

Accepted: 8 July 2026

Published online: 29 July 2026

Check for updates

Gwangmook Kim, Seokjoo Cho, Hyunah Ahn, Canran Wang, Hong Han, Xiaotian Ma, Moon-Ju Kim, Jin Qu, Jihong Min & Wei Gao

Hormones and metabolites jointly regulate physiology yet their dynamic interplay remains difficult to resolve due to the lack of technologies for continuous, multiplexed monitoring. Microneedle biosensors that access dermal interstitial fluid offer a minimally invasive approach to molecular profiling, but deployment is limited by trade-offs between fabrication scalability and precision, and by mechanical instability under skin deformation. Here we present a strain-isolated microneedle platform fabricated by combining two-photon polymerization with ultrasound-assisted moulding, enabling scalable replication of submicrometre-sharp microneedles (~430-nm apex width) bearing hierarchical, high-surface-area microstructures. Nanostructured gold and platinum electrodes enable high-fidelity sensing at the single-needle level, providing a 4.7-fold higher peak current and a 9-fold larger electrochemical surface area, respectively. Mechanical decoupling of the sensing interface from tissue deformation preserves stable molecular access during motion. When integrated with battery-free wireless electronics and multiplexed aptameric and enzymatic sensors, the system enables continuous in vivo monitoring of serotonin and glucose for 12 h. In freely moving rats, the platform captures biomolecular dynamics associated with stress, feeding and circadian rhythms. This work establishes a mechanically robust, scalable microneedle biointerface for ambulatory molecular monitoring and context-aware assessment of physiological state.

Human physiology is governed by dynamic interactions between hormonal signalling and metabolic regulation. Hormones serve as primary messengers that coordinate metabolic behaviour, while metabolites are functional outputs that feed back to modulate hormonal activity[1]. Such interactions ensure that physiological processes including digestion, immune regulation and energy utilization are precisely adjusted to fluctuating environments[2,3]. Because these pathways are tightly coupled and change over time, a single biomarker at a single time point provides only a fragmented view of the physiological state[4]. Consequently, decoding complex regulatory mechanisms and enabling personalized interventions requires technologies capable of simultaneous, continuous monitoring of both hormones and metabolites.

Wearable bioelectronics offer a promising route to such monitoring[5–13]. Dermal interstitial fluid (ISF) is a particularly attractive medium because its molecular composition closely reflects that of blood[14], the clinical gold standard. ISF is continuously accessible within the skin and is thus well suited for uninterrupted long-term molecular profiling (Fig. 1a). To interface with this biological reservoir, microneedle sensors have emerged as a minimally invasive platform[15]. Leveraging diverse transduction mechanisms, microneedle-based systems detect a wide array of biomarkers, including ions[16–18], metabolites[19–21], drugs[22–25],

Andrew and Peggy Cherng Department of Medical Engineering, Division of Engineering and Applied Science, California Institute of Technology, Pasadena, CA, USA. e-mail: weigao@caltech.edu

https://doi.org/10.1038/s41565-026-02247-5

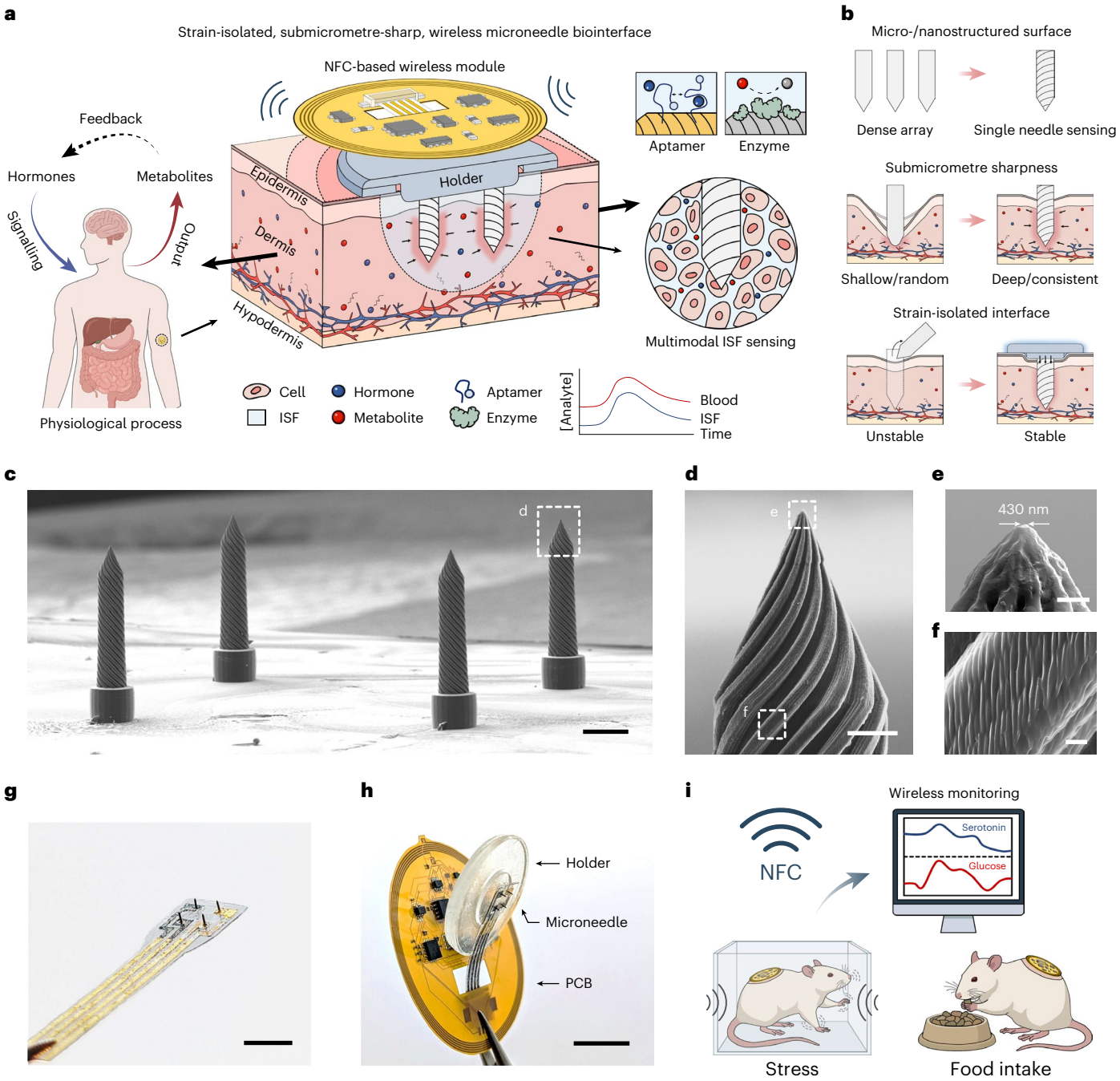

Fig. 1 | Strain-isolated microneedle biointerface for stable ambulatory monitoring of hormones and metabolites in ISF. a, Schematic illustration of the submicrometre-sharp, strain-isolated microneedle biointerface designed to monitor the dynamic interplay between hormonal signalling and metabolic regulation. The system integrates a multimodal microneedle array for ISF analysis, a strain-isolating holder for tissue interfacing and a battery-free NFC module for wireless data transmission. **b**, Conceptual comparison between a conventional microneedle interface (left) and the proposed strain-isolated interface (right), highlighting the use of high-surface-area, submicrometre-sharp microneedles and mechanical decoupling from skin deformation to enable stable, minimally invasive monitoring. **c**–**f**, SEM images of the fabricated microneedles, showing overview of the microneedle array layout (**c**), an individual microneedle (**d**), submicrometre tip sharpness (**e**) and nanotextured surface features (**f**). **g**,**h**, Photographs of the microneedle sensor patch (**g**) and the fully assembled wireless device integrating the microneedle array, strain-isolating holder and flexible printed circuit board (PCB) (**h**). **i**, Schematic of the in vivo experimental set-up for the real-time wireless monitoring of physiological responses during feeding and stress. Scale bars, 300 µm (**c**), 50 µm (**d**), 3 µm (**e**,**f**), 5 mm (**g**) and 1 cm (**h**).

hormones[26], nucleic acids[27,28] and proteins[29–31]. Integrated with miniaturized wireless electronics, these platforms enable real-time physiological tracking during daily activities, bridging the gap between episodic clinical testing and continuous health monitoring[32–34].

Despite these advances, ambulatory, long-term microneedle sensing remains limited by several fundamental challenges (Fig. 1b). First, many existing systems rely on dense microneedle arrays to achieve sufficient sensitivity, which increases invasiveness and pain while hindering penetration[35,36]. Second, fabrication imposes a trade-off between resolution and scalability[37]: high-throughput methods such as moulding or conventional three-dimensional (3D) printing often lack the precision to produce sufficiently sharp tips, causing shallow,

inconsistent penetration[38]. Third, their small dimensions limit mechanical retention in viscoelastic skin[36,39,40], so that routine motion can loosen or detach them and disrupt sensor–biofluid contact. Together, these limitations indicate that mechanical instability at the skin–sensor interface, rather than sensing chemistry alone, is a primary barrier to continuous ambulatory monitoring.

In this paper, we introduce a strain-isolated, submicrometre-precision microneedle platform integrated with battery-free near-field communication (NFC) electronics for consistent, minimally invasive biomolecular profiling. The platform combines two synergistic advances. First, a hybrid strategy pairing two-photon polymerization (TPP) with ultrasound-assisted moulding overcomes the conventional trade-off between resolution and scalability, enabling scalable production of microneedles with high-surface-area geometries and submicrometre-sharp tips (Fig. 1c–f). These features, together with nanostructured electrodes, support high-fidelity sensing at the single-needle level (Fig. 1g). Second, a strain-isolating biointerface mechanically decouples the local sensing microenvironment from macroscopic skin deformation, maintaining stable sensor–tissue coupling during movement and providing the foundation for continuous wireless monitoring under ambulatory conditions (Fig. 1h). By integrating multiplexed aptameric and enzymatic sensors, we continuously monitor serotonin (5-HT) and glucose, two biomarkers coupled through energy homeostasis and implicated in metabolic dysregulation[41]. In freely moving rats, continuous monitoring resolved distinct biomolecular dynamics associated with acute stress, feeding behaviour and circadian variation (Fig. 1i). Beyond this demonstration, the combination of scalable submicrometre fabrication and strain isolation provides a generalizable framework for decoding the dynamic interplay of hormonal and metabolic networks.

Scalable fabrication of submicrometre-sharp microneedles

To achieve precise and scalable microneedle fabrication, we integrated TPP 3D printing with an ultrasound-assisted moulding process (Fig. 2a,b). TPP provides submicrometre resolution and design freedom[30,42,43]. However, TPP alone is limited in speed and printable area, restricting scalable production. Although TPP masters can in principle be replicated via moulding, conventional approaches are hindered by incomplete cavity filling due to high viscosity, low wettability and entrapped air, which limits needle height, aspect ratio and tip fidelity[44].

Ultrasound-assisted moulding overcomes these barriers through two synergistic mechanisms. First, during ultrasonic agitation, the polydimethylsiloxane (PDMS) mould absorbs toluene, enhancing its surface wettability toward the polystyrene (PS)–toluene prepolymer (Supplementary Fig. 1). Second, ultrasonic cavitation collapses entrapped air bubbles and actively drives the viscous PS–toluene solution into deep and narrow mould cavities (Fig. 2c,d). This combined effect enables void-free filling of high-aspect-ratio cavities and intricate microstructures that are inaccessible using vacuum-, plasma- or centrifugation-based approaches. In contrast to the complete cavity filling observed for the toluene-conditioned mould (Fig. 2d), a control experiment performed without prior toluene conditioning revealed that a trapped air pocket remained within the deep cavity even after ultrasonic agitation, preventing complete cavity filling and successful microneedle replication (Supplementary Fig. 2). These results demonstrate that the toluene-induced wettability enhancement facilitates the complete filling of the high-aspect-ratio structures under ultrasound-assisted moulding.

The needle body was designed as a tapered cone (180-µm base diameter, 850-µm bare protruding height) decorated with continuous helical grooves along its axis (Fig. 2b). The recessed helical architecture increases the effective electrochemical surface area through 3D surface texturing while preserving a smooth macroscopic profile for reliable skin insertion and withdrawal.

We assessed the replication fidelity of this strategy by comparing it with conventional vacuum, plasma-treated and centrifugal casting techniques (Fig. 2e and Supplementary Table 1). Scanning electron microscopy (SEM) revealed that while alternative methods failed to produce the geometry of the high-aspect-ratio TPP master, ultrasound-assisted moulding achieved near-perfect replication. Notably, the submicrometre-sharp tip of the replicated microneedles (~430 nm) is important because tip sharpness directly influences insertion mechanics (Fig. 1e). The generality of this technique was further validated using conical moulds spanning a range of aspect ratios (Fig. 2f). Across all tested geometries, ultrasound-assisted moulding preserved tip sharpness and overall structure with minor height shrinkage (Fig. 2g and Extended Data Fig. 1), whereas conventional methods exhibited pronounced tip blunting and incomplete feature replication (Fig. 2h). The replication fidelity was further confirmed across five independent fabrication batches, with needle height and base width reproduced within ~1% variation and submicrometre tip sharpness preserved across all batches (Supplementary Fig. 3 and Supplementary Table 2). Importantly, the reusable PDMS mould and parallel needle formation during each sonication cycle enable scalable and low-cost production without repeated TPP fabrication (Supplementary Table 3).

To assess the functional implications of submicrometre tip sharpness, we evaluated microneedle insertion mechanics using multilayered skin phantoms composed of PDMS and agarose gel[36,45] (Supplementary Note 1). Compared with round microneedles (Supplementary Fig. 4), the submicrometre-sharp microneedles required approximately half of the insertion force and achieved nearly six-fold greater penetration depth (Fig. 2i–k). Crucially, while round needles failed to penetrate thicker PDMS layers, sharp microneedles consistently achieved deep and reproducible insertion across all tested thicknesses (Fig. 2l and Supplementary Figs. 5 and 6).

Finally, electrochemical characterization via cyclic voltammetry confirmed that the microstructured geometry increased the effective electrochemical surface area by 1.65-fold compared with plain needles (Fig. 2m). Notably, even plain TPP-fabricated microneedles exceeded geometric surface area predictions, probably due to intrinsic nanoscale textures introduced during TPP printing (Fig. 1f). These results indicate that the hierarchical integration of engineered microstructures with inherent nanoscale roughness maximizes the available sensing interface, enabling high-performance electrochemical sensing at the single-needle level (Fig. 2m, inset). In parallel, submicrometre tip sharpness reduces insertion force and tissue disruption, supporting stable penetration and sustained molecular access with a minimal number of microneedles.

Nanostructured sensors for hormonal and metabolic monitoring

To enable simultaneous monitoring of hormonal and metabolic signals, we integrated aptamer- and enzyme-based electrochemical sensors onto the microneedle array (Fig. 3a,b). For minimal invasiveness, each sensing channel is assigned to a single microneedle, in contrast to conventional dense microneedle arrays. Despite the reduced geometric footprint, high sensitivity is maintained by harnessing the submicrometre-precision microneedle fabrication that enables deep skin penetration and complex high-surface-area shape, together with nanostructured electrode interfaces formed by electrodeposited gold and nanoporous platinum (Fig. 3c).

Following integration with a polyethylene terephthalate (PET) substrate and metallization (Supplementary Figs. 7 and 8), the microneedles were functionalized with a 5-HT-specific aptamer[46,47] on electrodeposited gold. Binding of 5-HT induces a conformational change in the aptamer, modulating the electron transfer kinetics measured via square-wave voltammetry (SWV). Electrodeposition

https://doi.org/10.1038/s41565-026-02247-5

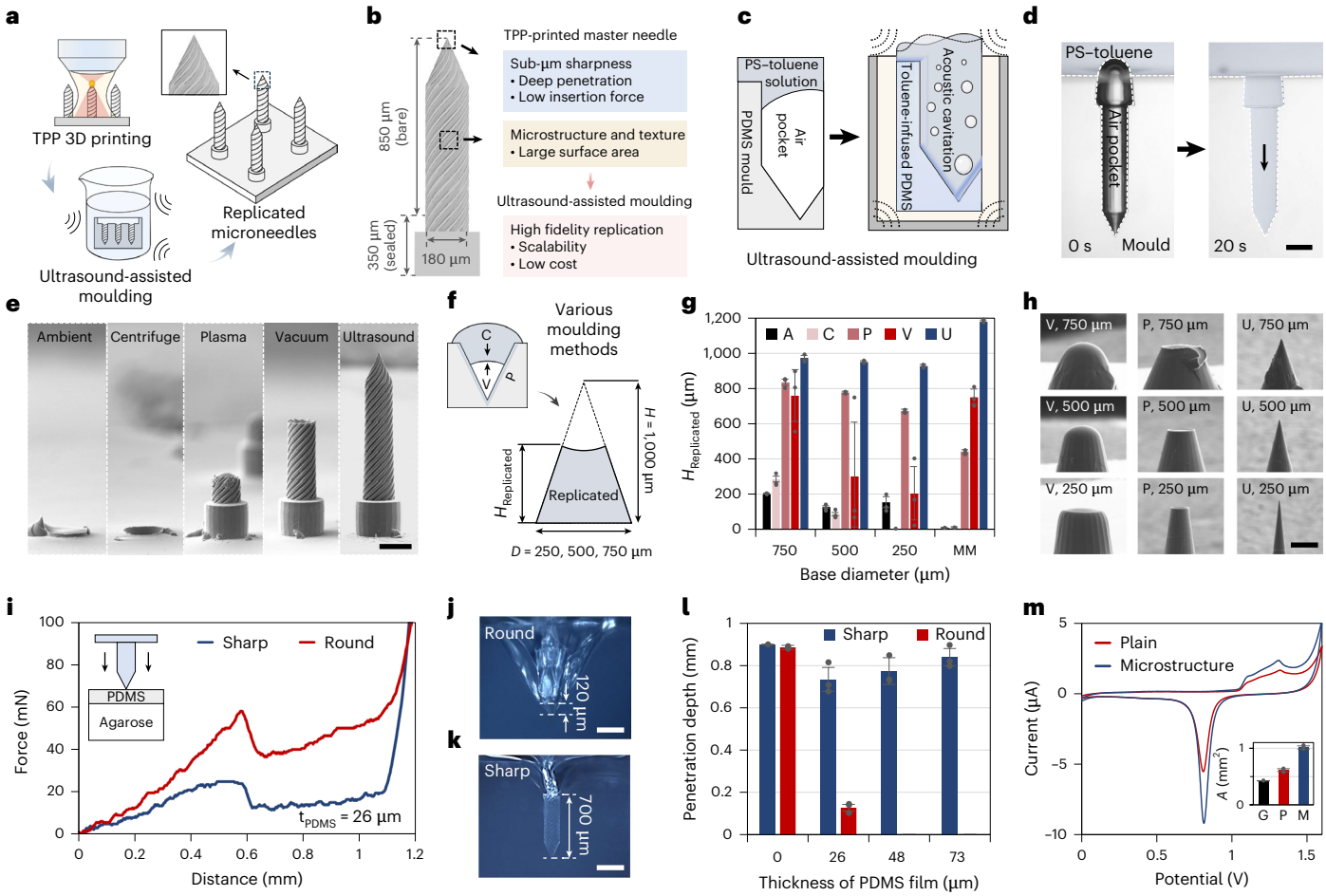

Fig. 2 | Design, scalable fabrication and functional characterization of submicrometre-sharp microneedles. a, Fabrication workflow combining TPP 3D printing of a master structure with ultrasound-assisted moulding for scalable high-fidelity replication. **b**, Microneedle design and strategies. **c**, Working principle of ultrasound-assisted moulding. **d**, Optical microscopy images comparing mould filling before (0 s) and after (20 s) ultrasound treatment. **e**, SEM comparison of microneedles replicated using different moulding methods. **f**, Conical microneedle geometries used to evaluate replication fidelity across moulding techniques. **g**, Replication height ($H_{Replicated}$) for conical microneedles with varying base diameters and for the proposed microstructured microneedle fabricated using ambient (A), centrifuging (C), plasma (P), vacuum (V) and ultrasound (U) methods. Error bars represent the s.d. of the mean ($n = 3$, independently fabricated microneedles). **h**, SEM images comparing tip sharpness of microneedles fabricated by vacuum, plasma and ultrasound-assisted moulding. **i**, Force–displacement curves comparing insertion mechanics of submicrometre-sharp microneedles and round-tipped microneedles (tip radius $r = 20$ μm). Inset: schematic of the insertion test using a multilayered skin phantom. **j**,**k**, Optical microscopy images showing penetration depths of round-tipped (**j**) and sharp-tipped (**k**) microneedles in a skin phantom. **l**, Quantitative comparison of penetration depths as a function of PDMS film thickness for sharp- and round-tipped microneedles. Error bars represent s.d. of the mean ($n = 3$, independent insertion tests, each using a separate microneedle). **m**, Cyclic voltammetry curves recorded in 0.05 M H_2SO_4 showing the gold redox features used to estimate the ECSA. Inset, ECSA comparison for geometric (G), plain (P) and microstructured (M) microneedles derived from the gold reduction peak charge. Scale bars, 200 μm (**d**,**e**), 100 μm (**h**) and 300 μm (**j**,**k**).

conditions were optimized to maximize surface area while suppressing dendritic growth, thereby preventing the release of metallic debris within the skin (Supplementary Fig. 9). Evaluation of the electrochemically active surface area (ECSA) before and after in vivo insertion confirmed that the nanostructured gold electrodes remained unchanged, with negligible variation in the ECSA (Supplementary Fig. 10a–d). The combination of microstructured geometry and nanostructured gold yielded a 4.7-fold increase in SWV peak current compared with plain gold microneedles (Fig. 3d).

The 5-HT sensor exhibited a concentration-dependent decrease in SWV peak current (Fig. 3e). To compensate for baseline drift and environmental fluctuations, we used a kinetic differential measurement (KDM)[48] derived from SWV responses at 10 Hz (off-signal) and 30 Hz (on-signal) (Supplementary Figs. 11 and 12). This optimized approach yielded a monotonic calibration curve across the physiological concentration range (Fig. 3f). Repeated regeneration experiments demonstrated stable 5-HT sensing over 20 cycles, confirming the reversibility of the aptamer-functionalized interface under repeated electrochemical interrogation (Fig. 3g).

For glucose sensing, a nanoporous platinum electrode provided a 9-fold increase in effective electrochemical surface area compared with non-porous platinum (Fig. 3h and Supplementary Fig. 13). Depth-resolved energy-dispersive X-ray spectroscopy (EDS) analysis confirmed effective surface dealloying, with residual aluminium detected only within the bulk platinum matrix (Supplementary Fig. 14). The sensor operates through direct electrochemical oxidation of enzymatically generated H_2O_2 on the nanoporous platinum surface without the use of a redox mediator. After functionalization with glucose oxidase embedded in a chitosan matrix and protected by a Nafion layer, the sensor demonstrated a concentration-dependent amperometric response (Fig. 3i). The Nafion overcoat further enhances selectivity by acting as a permselective barrier[49] that suppresses transport of anionic interferents such as ascorbate and urate while allowing H_2O_2 generated by the enzymatic reaction to reach the platinum surface for electrochemical

https://doi.org/10.1038/s41565-026-02247-5

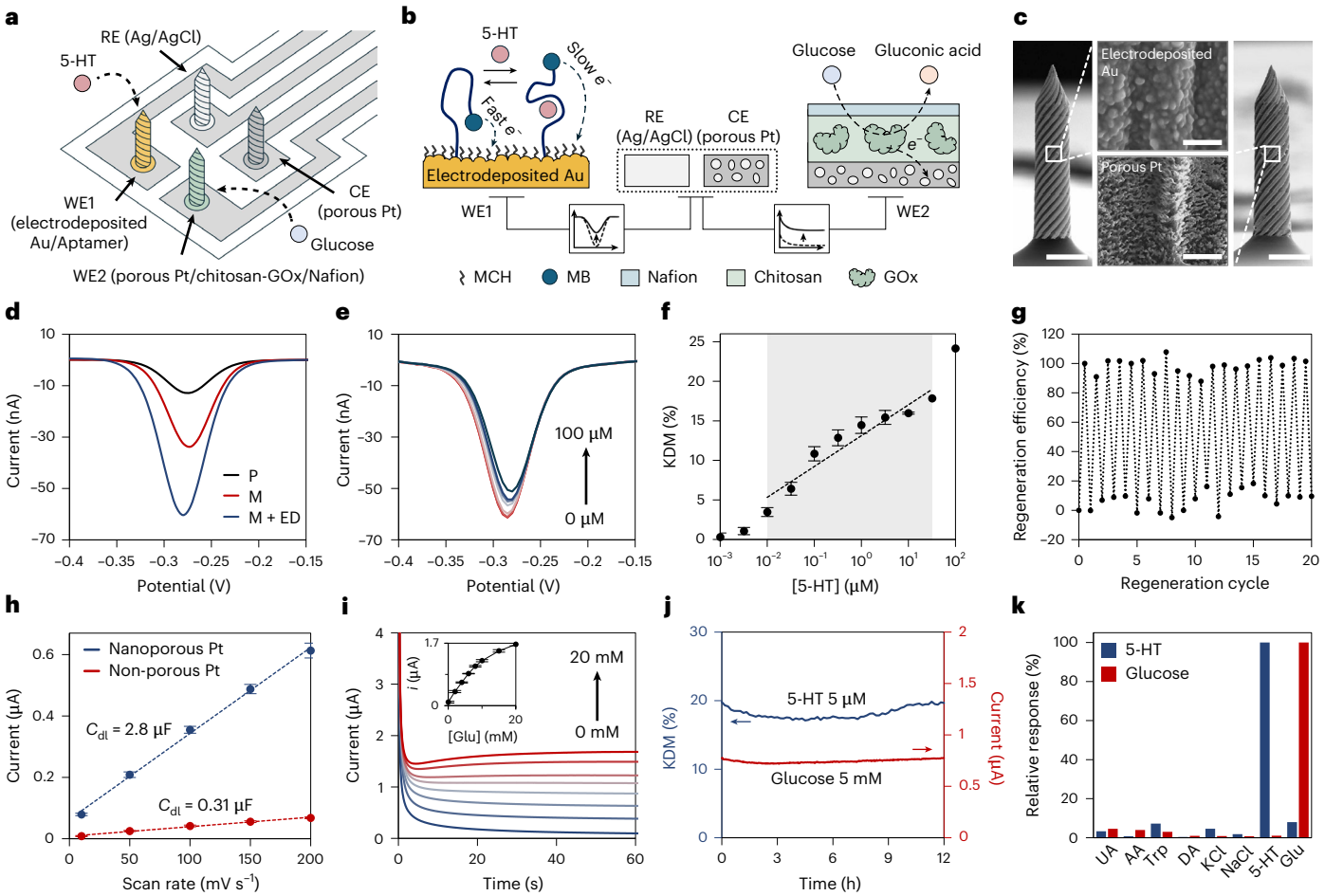

Fig. 3 | Design and electrochemical characterization of serotonin (5-HT) and glucose microneedle sensors. a, Architecture of the multiplexed microneedle sensing array, comprising a 5-HT working electrode (WE1), a glucose working electrode (WE2), a reference electrode (RE) and a counter-electrode (CE). **b**, Schematic illustration of the sensing principles of the aptameric 5-HT sensor and the enzymatic glucose sensor. **c**, SEM images of the microneedle electrode. Insets: nanostructured electrode surface formed by electrodeposited Au (top) and nanoporous Pt (bottom). Scale bars, 200 µm (microneedles) and 500 nm (insets). **d**, SWV responses in PBS (pH 7.4) at 10 Hz, comparing plain (P), microstructured (M) and microstructured plus electrodeposited (M + ED) microneedle electrodes. **e**, SWV responses of the 5-HT sensor measured at increasing 5-HT concentrations (0–100 µM). **f**, Calibration of the KDM, derived from SWV responses at 10 and 30 Hz, as a function of 5-HT concentration. The shaded region denotes the physiologically relevant concentration range (10 nM–30 µM) considered in this study. Error bars represent the s.d. of the mean (n = 3, independently fabricated sensors). Dotted line represents the linear fit of the calibration data points. **g**, Regeneration stability of the 5-HT sensor during repeated cycling between 0 and 5 µM 5-HT solutions in PBS (pH 7.4) following 1 h pre-equilibration in PBS. Regeneration efficiency was normalized to the KDM response of the first regeneration cycle (KDM/KDM_0). **h**, Capacitive current as a function of scan rate for nanoporous platinum and non-porous platinum electrodes. C_{dl}, electrochemical double-layer capacitance derived from the linear slope. Error bars represent the s.d. of the mean (n = 3, independently prepared electrodes). **i**, Chronoamperometric responses of the glucose sensor to increasing glucose concentrations (0–20 mM) in PBS (pH 7.4). Inset: calibration plot of steady-state current measured at 60 s. Error bars represent the s.d. of the mean (n = 3, independently fabricated sensors). **j**, Long-term signal stability of the 5-HT and glucose sensors measured over 12 h in solution containing 5 µM 5-HT and 5 mM glucose. **k**, Selectivity of the 5-HT and glucose sensors measured against common potential interferents in ISF, including uric acid (UA, 100 µM), ascorbic acid (AA, 100 µM), tryptophan (Trp, 100 µM), dopamine (DA, 500 pM), KCl (1 mM) and NaCl (1 mM), relative to target 5-HT (1 µM) and glucose (Glu, 5 mM).

oxidation. Similar to the gold electrodes, the porous platinum electrodes exhibited negligible changes in electrochemical double-layer capacitance following in vivo insertion, indicating preservation of the nanostructured surface architecture (Supplementary Fig. 10e–h).

The feasibility for continuous multiplexed monitoring was evaluated by assessing long-term sensor stability over a 12-h period (Fig. 3j). Selectivity testing confirmed minimal interference from common ISF constituents, including uric acid, ascorbic acid and electrolytes (Fig. 3k). Furthermore, sequential spiking experiments demonstrated that each sensing channel responded selectively to its target analyte while exhibiting negligible response to changes in the other analyte (Supplementary Fig. 15).

Sensor performance was further validated in a physiologically relevant matrix using serum (Supplementary Fig. 16). Direct comparison of the calibration curves in buffer (Fig. 3f,i) and serum (Supplementary Fig. 16a,b) showed that both sensors preserved their characteristic concentration-dependent responses in the physiological matrix, albeit with somewhat reduced apparent sensitivities. These differences are consistent with matrix effects associated with the physiological serum environment, including endogenous analytes and non-specific interfacial interactions. Long-term monitoring in serum over 12 h revealed sensor-specific stabilization behaviours (Supplementary Fig. 17). The 5-HT sensor exhibited an initial equilibration phase followed by a quasi-stable operating regime, whereas the glucose sensor showed minimal signal variation throughout the incubation period. These differences are consistent with the distinct sensing mechanisms and interfacial architectures of the two sensors.

https://doi.org/10.1038/s41565-026-02247-5

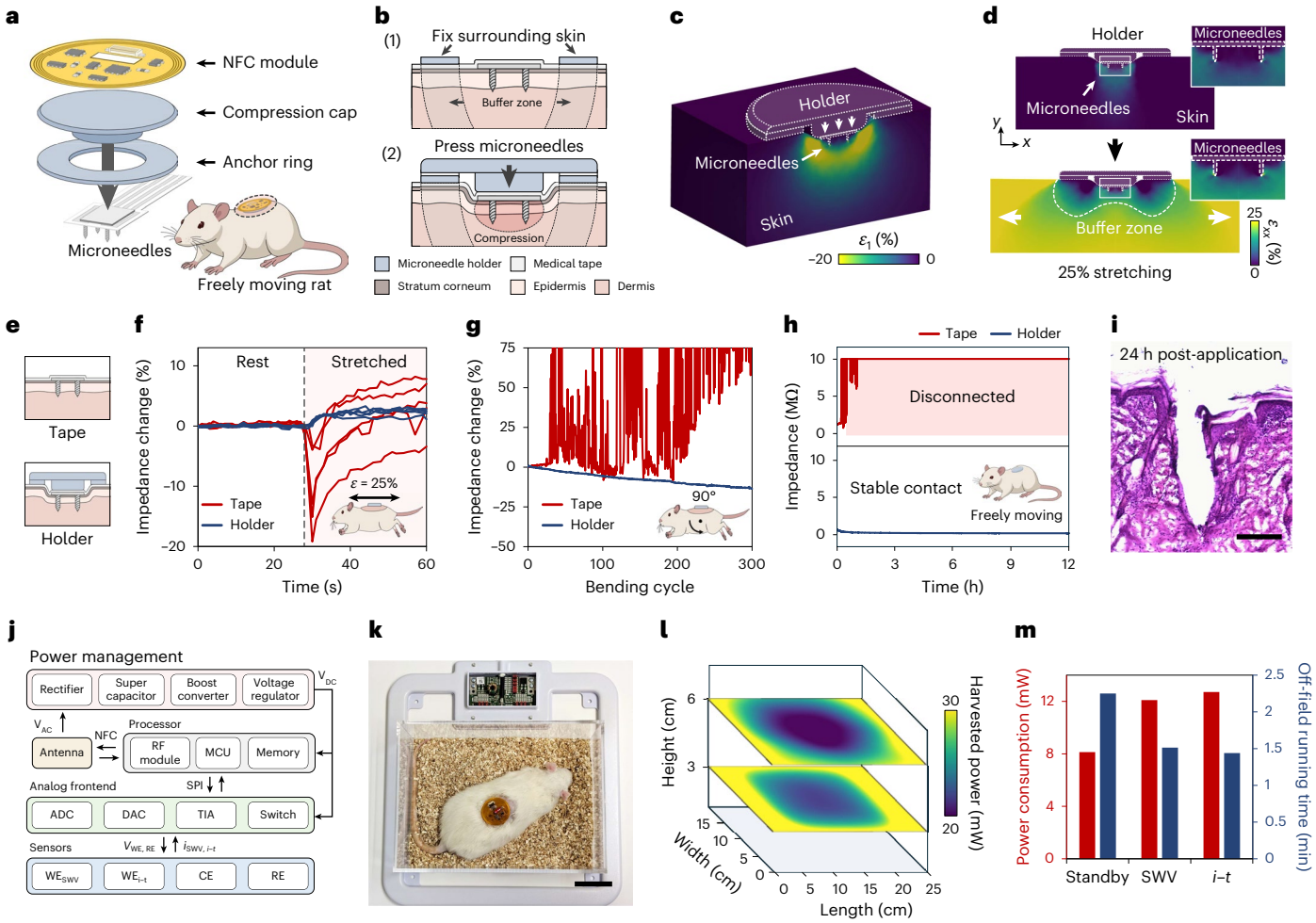

Fig. 4 | Strain-isolating biointerface and wireless system for stable ambulatory microneedle sensing. a, Exploded view of the strain-isolating assembly, showing integration of the microneedle array with the anchor ring, compression cap and battery-free NFC module. **b**, Cross-sectional schematics illustrating the two-step attachment process: (1) fixation of surrounding skin to define a localized strain-buffering zone and facilitate microneedle insertion, and (2) application of sustained compressive loading to maintain stable microneedle–tissue contact. **c**, FEA showing the distribution of maximum principal strain on the skin surface with the strain-isolating holder in place. **d**, Cross-sectional strain profiles along the stretching direction (ε_{xx}) at rest (top) and under 25% macroscopic skin stretching (bottom). Insets: magnified views of the local strain environment near the microneedles. **e**, Cross-sectional schematics comparing conventional medical tape and the proposed strain-isolating holder configurations. **f**, In vivo assessment of contact stability on rat dorsal skin, comparing relative impedance changes (100 Hz) for microneedles with and without the strain-isolating holder under 25% applied tensile strain ($n = 5$, repeated measurements). **g**, Relative impedance changes during repeated 90° bending cycles for tape and holder attachments. **h**, Continuous impedance monitoring over 12 h in a freely moving rat. **i**, H&E-stained cross-section of rat skin immediately after device removal following 24 h of continuous application in a freely moving animal. Scale bar, 200 µm. **j**, Block diagram of the wireless electronic system, including power management, processor, analogue front-end and sensor interface units. ADC, analogue-to-digital converter; DAC, digital-to-analogue converter; TIA, transimpedance amplifier; MCU, microcontroller unit; SPI, serial peripheral interface. **k**, Photograph of the in vivo experimental set-up showing a freely moving rat within a cage surrounded by a transmitting antenna. Scale bar, 5 cm. **l**, Spatial distribution of harvested power within the cage at different heights, measured at a radiofrequency (RF) transmission power of 8 W. **m**, Power consumption and off-field operating times enabled by a 0.5-F supercapacitor for different operation modes, including standby, SWV and amperometry (*i*–*t*).

Strain-isolating biointerface and wireless system for ambulatory stability

To enable reliable long-term sensing in freely moving subjects, we developed a strain-isolating biointerface integrated with a battery-free NFC electronic system (Fig. 4a and Extended Data Fig. 2). The holder establishes a mechanically decoupled sensing zone through two coordinated elements: an anchor ring and a compression cap (Fig. 4b). The anchor ring tautens and fixes the surrounding skin, creating a localized buffer zone that isolates the sensing region from external strain. Concurrently, the compression cap applies a constant downward load, ensuring deep and stable microneedle insertion and sustained tissue contact.

Finite element analysis (FEA) corroborated this strain-isolating mechanism. Simulations showed that the holder maintains a compressive load at the sensing site (Fig. 4c) while decoupling the microneedle–tissue interface from externally applied stretching (Fig. 4d and Supplementary Fig. 18). As a result, the local strain environment experienced by the microneedles remained mostly unchanged even under 25% macroscopic skin stretching, thereby minimizing motion-induced artefacts (Fig. 4d, insets).

The mechanical effectiveness of this interface is further enhanced by minimizing the number of microneedles within the compressed region (Extended Data Fig. 3a). Under a rigid indenter, compressive force concentrates near the edges of the contact area. In dense arrays with large contact area, central needles experience insufficient vertical strain for stable engagement. In a sparse array with narrow contact area (for example, 2 × 2), all needles sit near the periphery of the

compression cap, where compressive strain is maximized. FEA confirmed that this geometry generates substantially larger vertical strain (ε_{zz}) beneath each microneedle (Extended Data Fig. 3b,c), providing a mechanical basis for the single-needle-per-function design, which simultaneously enhances stability and minimizes invasiveness.

The strain-isolating biointerface was validated in vivo on rat dorsal skin (Fig. 4e,f and Extended Data Fig. 4a–c). Under applied tensile and compressive strains, tape-secured sensors exhibited impedance fluctuations up to 20%, indicating unstable contact. In contrast, holder-integrated sensors showed negligible variation, confirming mechanical decoupling from skin deformation. Furthermore, while both tolerated a single 90° static bend (~2% change, Extended Data Fig. 4b), under cyclic bending (90°, 0.5 Hz, post-mortem rat), tape-secured sensors failed rapidly, whereas the holder maintained stable contact (Fig. 4g). Under high-frequency vibration (1,000 r.p.m., post-mortem rat), both remained connected, but the tape-secured sensor showed a gradual impedance increase whereas the holder remained stable (Extended Data Fig. 4d,e). Long-term reliability was then evaluated in freely moving rats over 12 h (Fig. 4h). Whereas tape-secured microneedles lost contact within ~25 min, as evidenced by continuously rising impedance (Supplementary Fig. 19a), the microneedles secured with the strain-isolating biointerface maintained stable electrical contact throughout the entire monitoring duration. Notably, the impedance gradually decreased and stabilized over time, consistent with progressive interface settling (Supplementary Fig. 19b).

To confirm sustained insertion depth during ambulatory operation, we performed histological and macroscopic analyses after 24 h of continuous application in freely moving rats (Fig. 4i and Extended Data Fig. 5). Cross-sectional haematoxylin and eosin (H&E) images confirmed that the microneedles remained embedded within the dermis throughout the 24-h monitoring period (Extended Data Fig. 5b). After microneedle removal, a distinct needle-shaped microchannel was observed (Fig. 4i). No apparent signs of severe acute inflammation, haemorrhage or tissue disruption were observed around the insertion site. Unlike the immediate viscoelastic closure after transient punctures (Extended Data Fig. 5a,c), the post-24-h sites showed substantially delayed recovery, requiring ~12 h for macroscopic closure (Extended Data Fig. 5d). These observations are consistent with prolonged and stable tissue engagement under ambulatory conditions.

For untethered operation, the sensors were integrated with a battery-free NFC wireless system for power delivery and data transmission (Fig. 4j and Supplementary Fig. 20). The system comprises an NFC reader, a transmitting antenna and miniaturized NFC electrochemical modules (Fig. 4k and Supplementary Fig. 21). Both the antenna and the NFC module were tuned to 13.56 MHz to maximize power transfer efficiency (Supplementary Fig. 22). The cage configuration provided harvested power exceeding 20 mW throughout the monitoring area (Fig. 4l).

To ensure operation during transient power interruptions, a supercapacitor was incorporated as an auxiliary energy buffer (Supplementary Fig. 23). This design enables stable off-field operation while maintaining active sensing modes (Fig. 4m). To preserve data integrity in awake animals, we implemented a hardware–software signal processing and restoration workflow to mitigate artefacts from abrupt motion, shivering or mechanical interference with the NFC module (Supplementary Note 2 and Supplementary Figs. 24 and 25). Together, this integrated mechanical, electronic and computational architecture ensures continuous biochemical monitoring in freely moving subjects (Supplementary Fig. 26 and Supplementary Video 1).

Wireless multiplexed monitoring of hormonal and metabolic dynamics in vivo

To demonstrate the practical utility of the wireless microneedle platform, we monitored real-time dynamics of 5-HT and glucose under multiple physiological conditions. 5-HT acts as an endocrine regulator of glucose homeostasis by modulating hepatic glucose production and uptake, while also facilitating glucose-stimulated insulin secretion[41]. Dysregulation of this metabolic axis is implicated in metabolic disorders, including type 2 diabetes[50] and obesity[51]. Meanwhile, 5-HT levels are susceptible to stress through mechanisms involving platelet-mediated release[52,53], altered tryptophan metabolism[54] and gut microbiota[55]. Similarly, glucose is influenced by stress-induced hyperglycaemia[56]. These interdependencies motivate simultaneous time-resolved monitoring to deconvolve the biomarker dynamics[1] (Fig. 5a).

We first characterized the in vivo stabilization behaviour of the sensors. Following insertion into rat dorsal skin, both 5-HT and glucose sensors exhibited a gradual decay in signal intensity, approaching a quasi-stable state after ~120 min[22,25,57] (Supplementary Figs. 27 and 28). This drift is consistent with sensor–tissue equilibration, potentially including wound healing, biofouling and biointerface adaptation at the insertion site[57–60] (Supplementary Fig. 29). Although the decay kinetics varied between animals, all sensors converged toward a quasi-stable operating regime.

To verify that prolonged wear does not compromise sensing performance, rats were allowed unrestricted movement for 24 h with the sensors in place, followed by a 5-HT injection challenge (Fig. 5b). After 24 h, although the absolute SWV peak current of the 5-HT sensor decreased, the characteristic peak features remained well defined, while the glucose sensor maintained a stable amperometric response (Supplementary Fig. 30). Upon injection, the microneedle sensors captured a rapid rise in interstitial 5-HT levels accompanied by a decrease in glucose concentration, consistent with 5-HT-induced hypoglycaemia[61] (Fig. 5c). The profiles matched reference measurements obtained using enzyme-linked immunosorbent assay (ELISA) and a commercial glucometer. These results were comparable to those obtained in injection tests conducted without the preceding free-movement period (Supplementary Fig. 31), indicating that the strain-isolating biointerface preserves sensor functionality and stable tissue contact after extended ambulatory use.

All in vivo experiments followed a standardized workflow (Fig. 5d). A 4-h prestabilization period allowed the animal to recover from anaesthesia and bypassed the rapid initial equilibration phase

Fig. 5 | In vivo validation and wireless multiplexed monitoring of 5-HT and glucose dynamics in freely moving rats. a, Schematic illustration of physiological pathways involving 5-HT (blue) and glucose (red) engaged during acute stress and food intake. GI, gastrointestinal; EC, enterochromaffin. **b**, Experimental workflow for in vivo sensor stability, including a 24-h free-movement period followed by a 5-HT injection challenge. **c**, Representative real-time sensor response to 5-HT injection after 24 h of unrestricted movement. Coloured circles and solid lines represent raw signals and smoothed traces, respectively. Black dots and dashed lines indicate reference concentrations measured by ELISA (serum 5-HT) and a glucometer (blood glucose). **d**, Timeline of in vivo experimental procedures. **e**,**f**, Correlation between microneedle sensor outputs and reference measurements for serum 5-HT (ELISA, log–log scale) (**e**) and blood glucose (glucometer, linear scale) (**f**). Dashed lines indicate regression fits (**e**, $\log y = 0.81 \times \log x + 0.09$; **f**, $y = 0.78 \times x + 2.40$). Validation was performed on $n = 64$ paired measurements obtained from 11 rats (9 physiological monitoring experiments and 2 5-HT injection studies). R^2 and mean absolute relative difference (MARD) values are displayed on the plot. **g**, Schematic of the acute stress protocol induced by cage tapping noise. **h**, Simultaneous real-time monitoring of interstitial 5-HT and glucose dynamics during acute stress in three animals (rats 1–3). Red shaded areas indicate the stress stimulus period. **i**, Schematic of the feeding experiment following 24-h fasting. **j**, Simultaneous real-time monitoring of interstitial 5-HT and glucose dynamics during food intake in three animals (rats 4–6). Arrows indicate the feeding event. **k**, Schematic of the 12-h diurnal monitoring experiment. **l**, Representative 12-h wireless monitoring of interstitial 5-HT and glucose dynamics during unrestricted behaviour (rat 7).

https://doi.org/10.1038/s41565-026-02247-5

of the sensors (Supplementary Figs. 27 and 28). As shown in the postinsertion sensitivity test (Supplementary Fig. 32), the residual sensitivity variation over the subsequent 12-h measurement window (4–16 h postinsertion) remains within ~6% and ~15% for the 5-HT and glucose sensors, respectively. For extended recordings such as the feeding and 12-h experiments, the gradual baseline current drift of the glucose sensor was further corrected by linear subtraction (Supplementary Fig. 33). For the 5-HT sensor, the KDM method effectively compensates for long-term SWV peak drift and non-specific baseline variations (Supplementary Fig. 34). Based on the postinsertion sensitivity analysis (Supplementary Fig. 32), the practical operating lifetime of the current platform is approximately 1 day.

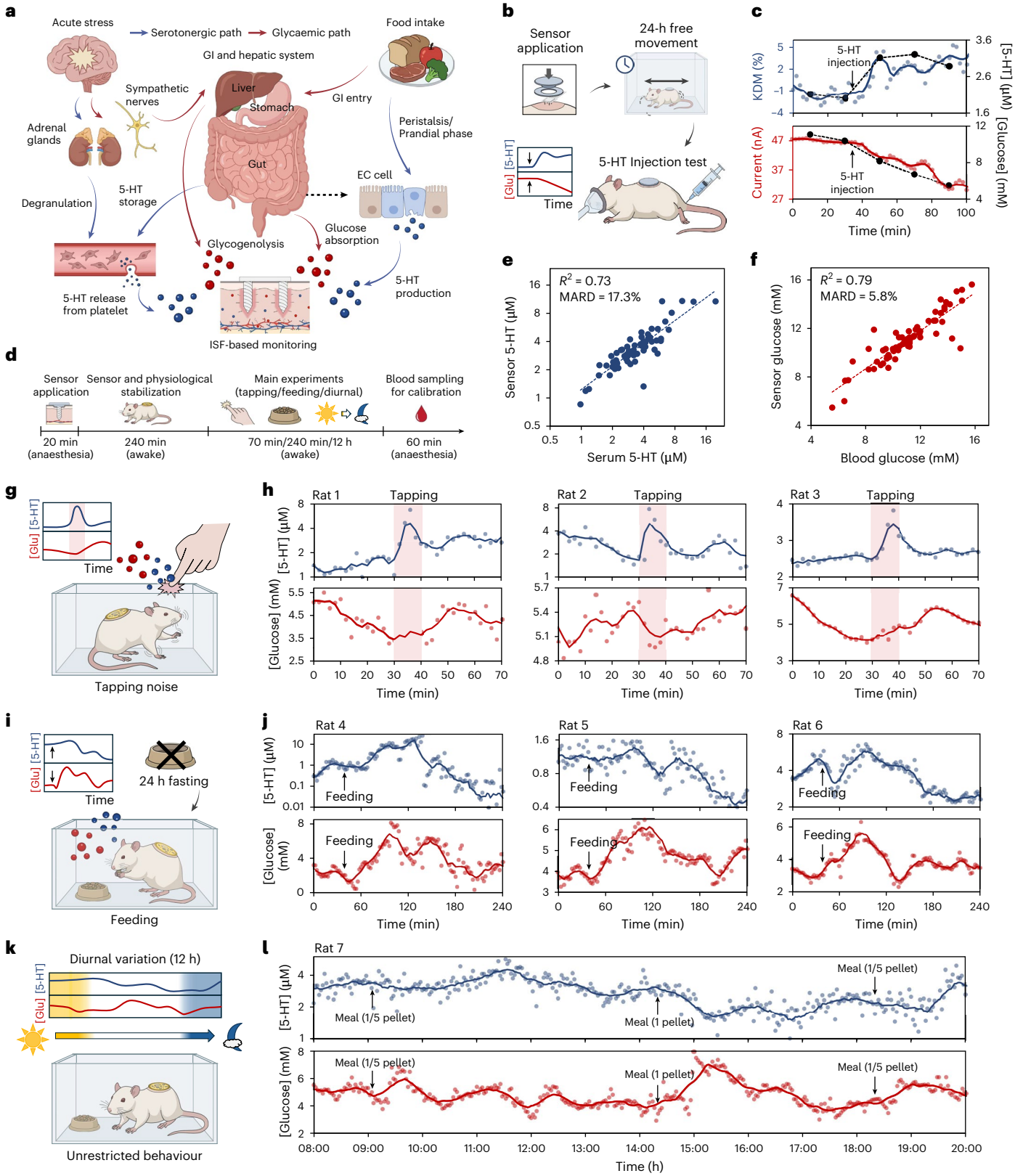

In the final step, blood samples were collected and used to correlate sensor outputs with reference concentrations (Supplementary Fig. 35). Although exact insertion depth may vary across animals, the combination of post–in vivo calibration and mechanically stabilized insertion minimizes the influence of this variability on sensor readout, supporting reliable translation of sensor signals into biomolecular dynamics under ambulatory conditions. The validation plots demonstrated agreement between sensor signals and reference measurements (Fig. 5e,f). The estimated 5-HT levels fall within the range previously reported for peripheral 5-HT measurements in rodents[52,53,62,63].

We first evaluated the platform's ability to resolve acute stress responses using cage tapping as a stressor (Fig. 5g). Both biomarkers exhibited synchronized increases following stimulation but with distinct temporal profiles (Fig. 5h). Interstitial 5-HT displayed a rapid and transient spike, potentially reflecting platelet-mediated release triggered by sympathetic activation[52,64]. In contrast, glucose levels rose more gradually and persisted longer, consistent with stress-induced hepatic glycogenolysis and gluconeogenesis[56].

Next, we investigated postprandial dynamics following a 24-h fast (Fig. 5i). Prior to feeding, baseline 5-HT levels were elevated, consistent with the upregulation of gut-derived 5-HT during deprivation[62]. Upon food intake, glucose levels increased rapidly, while 5-HT exhibited transient fluctuations followed by a gradual decline (Fig. 5j). These fluctuations may reflect mechanical stimulation of enterochromaffin cells during food passage[2], whereas the overall downward trend aligns with restored energy homeostasis as fasting-associated serotonergic signalling returns toward basal levels.

Finally, continuous monitoring over a 12-h period captured diurnal variation during unrestricted activity (Fig. 5k,l and Extended Data Fig. 6). Interstitial 5-HT levels followed a pronounced circadian pattern, characterized by elevated levels in the early morning, a midday trough and a subsequent evening rise, consistent with previous reports[65]. This trend was observed across all three animals, although the precise timing and magnitude varied between individuals. In contrast, glucose dynamics were more influenced by feeding behaviour. While glucose levels spiked following food consumption, 5-HT levels did not show a consistent meal-dependent response. Small meals (for example, 1/5 pellet) produced negligible changes in 5-HT. Although larger meals (for example, 1 pellet) were associated with fluctuations and a gradual decrease over several hours, these trends remained aligned with the underlying circadian trajectory toward the midday trough[62,65].

Collectively, our platform resolves distinct biomolecular dynamics associated with stress, fasting and circadian regulation by capturing the kinetic interplay between 5-HT and glucose. We emphasize that these findings represent a pilot-scale demonstration of platform capability rather than definitive physiological mapping.

Conclusion

We developed submicrometre-precise, strain-isolated microneedles that establish mechanical decoupling, enabling minimally invasive interstitial fluid access at the single-needle level under free movement. Important challenges nevertheless remain. First, while microneedle fabrication is scalable and precise, functionalizing the sensing layers still requires multiple time-consuming processes such as metallization and incubation. Facile on-microneedle functionalization or efficient off-needle sensing architectures would offer a solution. Second, the operating lifetime is currently limited to ~1 day by interfacial biofouling and biorecognition-molecule degradation, which will require more efficient antifouling interfaces and biorecognition molecules with improved stability. Third, standardized ISF calibration protocols and ultimately calibration-free sensing strategies will be essential for fully quantitative, subject-independent monitoring.

Online content

Any methods, additional references, Nature Portfolio reporting summaries, source data, extended data, supplementary information, acknowledgements, peer review information; details of author contributions and competing interests; and statements of data and code availability are available at https://doi.org/10.1038/s41565-026-02247-5.

References

1. Güntner, A. T. et al. Challenges and opportunities of wearable molecular sensors in endocrinology and metabolism. *Nat. Rev. Endocrinol.* **22**, 50–60 (2026).
2. Mawe, G. M. & Hoffman, J. M. Serotonin signalling in the gut—functions, dysfunctions and therapeutic targets. *Nat. Rev. Gastroenterol. Hepatol.* **10**, 473–486 (2013).
3. Spohn, S. N. & Mawe, G. M. Non-conventional features of peripheral serotonin signalling—the gut and beyond. *Nat. Rev. Gastroenterol. Hepatol.* **14**, 412–420 (2017).
4. Sempionatto, J. R., Lasalde-Ramírez, J. A., Mahato, K., Wang, J. & Gao, W. Wearable chemical sensors for biomarker discovery in the omics era. *Nat. Rev. Chem.* **6**, 899–915 (2022).
5. Brasier, N. et al. Applied body-fluid analysis by wearable devices. *Nature* **636**, 57–68 (2024).
6. Heng, W. et al. A smart mask for exhaled breath condensate harvesting and analysis. *Science* **385**, 954–961 (2024).
7. Zhang, B. et al. A three-dimensional liquid diode for soft, integrated permeable electronics. *Nature* **628**, 84–92 (2024).
8. Shi, J. et al. Active biointegrated living electronics for managing inflammation. *Science* **384**, 1023–1030 (2024).
9. Lee, H. et al. A graphene-based electrochemical device with thermoresponsive microneedles for diabetes monitoring and therapy. *Nat. Nanotechnol.* **11**, 566–572 (2016).
10. Xu, Y. et al. Phase-separated porous nanocomposite with ultralow percolation threshold for wireless bioelectronics. *Nat. Nanotechnol.* **19**, 1158–1167 (2024).
11. Kim, J. et al. A soft and transparent contact lens for the wireless quantitative monitoring of intraocular pressure. *Nat. Biomed. Eng.* **5**, 772–782 (2021).
12. Cho, S. et al. Wearable lateral flow assays for cortisol monitoring with time-dynamic sweat sampling and sensing by electrochromic timers. *Nat. Sens.* **1**, 85–98 (2026).
13. Kwon, S. et al. At-home wireless sleep monitoring patches for the clinical assessment of sleep quality and sleep apnea. *Sci. Adv.* **9**, eadg9671 (2023).
14. Friedel, M. et al. Opportunities and challenges in the diagnostic utility of dermal interstitial fluid. *Nat. Biomed. Eng.* **7**, 1541–1555 (2023).
15. Vora, L. K. et al. Microneedle-based biosensing. *Nat. Rev. Bioeng.* **2**, 64–81 (2024).
16. Lee, W. et al. Conformable microneedle pH sensors via the integration of two different siloxane polymers for mapping peripheral artery disease. *Sci. Adv.* **7**, eabi6290 (2021).
17. Yang, J. et al. Masticatory system–inspired microneedle theranostic platform for intelligent and precise diabetic management. *Sci. Adv.* **8**, eabo6900 (2022).
18. Zheng, Y. et al. A wearable microneedle-based extended gate transistor for real-time detection of sodium in interstitial fluids. *Adv. Mater.* **34**, 2108607 (2022).
19. Bai, J. et al. Coin-sized, fully integrated, and minimally invasive continuous glucose monitoring system based on organic electrochemical transistors. *Sci. Adv.* **10**, eadl1856 (2024).
20. Ausri, I. R. et al. Multifunctional dopamine-based hydrogel microneedle electrode for continuous ketone sensing. *Adv. Mater.* **36**, 2402009 (2024).
21. Ashraf, G. et al. Microneedle-integrated FePc–MOF–MXene nanozyme patch for in vivo L-cysteine monitoring. *Adv. Mater.* **37**, 2502804 (2025).

22. Wu, Y. et al. Microneedle aptamer-based sensors for continuous, real-time therapeutic drug monitoring. *Anal. Chem.* **94**, 8335–8345 (2022).
23. Lin, S. et al. Wearable microneedle-based electrochemical aptamer biosensing for precision dosing of drugs with narrow therapeutic windows. *Sci. Adv.* **8**, eabq4539 (2022).
24. Yang, J. et al. Microneedle-based integrated pharmacokinetic and pharmacodynamic evaluation platform for personalized medicine. *Nat. Commun.* **16**, 6260 (2025).
25. Booth, M. A. et al. Pilot phase clinical trial of a wearable, electrochemical aptamer-based patch for continuous drug concentration measurement. *Nat. Biotechnol*. https://doi.org/10.1038/s41587-026-03010-w (2026).
26. GhavamiNejad, A. et al. Continuous insulin monitoring using an antibody-protecting zwitterionic microneedle patch. *Nat. Biomed. Eng*. https://doi.org/10.1038/s41551-025-01477-7 (2025).
27. Al Sulaiman, D. et al. Hydrogel-coated microneedle arrays for minimally invasive sampling and sensing of specific circulating nucleic acids from skin interstitial fluid. *ACS Nano* **13**, 9620–9628 (2019).
28. Yang, B., Kong, J. & Fang, X. Programmable CRISPR-Cas9 microneedle patch for long-term capture and real-time monitoring of universal cell-free DNA. *Nat. Commun.* **13**, 3999 (2022).
29. Wang, Z. et al. Microneedle patch for the ultrasensitive quantification of protein biomarkers in interstitial fluid. *Nat. Biomed. Eng.* **5**, 64–76 (2021).
30. Zargartalebi, H. et al. Active-reset protein sensors enable continuous in vivo monitoring of inflammation. *Science* **386**, 1146–1153 (2024).
31. Lin, Z.-T. et al. Wearable photonic device for multiple biomarker sampling and detection without blood draws. *Adv. Mater.* **37**, 2416240 (2025).
32. Tehrani, F. et al. An integrated wearable microneedle array for the continuous monitoring of multiple biomarkers in interstitial fluid. *Nat. Biomed. Eng.* **6**, 1214–1224 (2022).
33. Zhu, B. et al. A wearable integrated microneedle electrode patch for exercise management in diabetes. *Research* **7**, 0508 (2024).
34. Chang, A.-Y. et al. Integration of chemical and physical inputs for monitoring metabolites and cardiac signals in diabetes. *Nat. Biomed. Eng*. **10**, 94–109 https://doi.org/10.1038/s41551-025-01439-z (2025).
35. Gill, H. S., Denson, D. D., Burris, B. A. & Prausnitz, M. R. Effect of microneedle design on pain in human volunteers. *Clin. J. Pain* **24**, 585–594 (2008).
36. Makvandi, P. et al. Engineering microneedle patches for improved penetration: analysis, skin models and factors affecting needle insertion. *Nano-Micro Lett.* **13**, 93 (2021).
37. Kim, G., Ahn, H., Chaj Ulloa, J. & Gao, W. Microneedle sensors for dermal interstitial fluid analysis. *Med-X* **2**, 15 (2024).
38. Römgens, A. M., Bader, D. L., Bouwstra, J. A., Baaijens, F. P. T. & Oomens, C. W. J. Monitoring the penetration process of single microneedles with varying tip diameters. *J. Mech. Behav. Biomed. Mater.* **40**, 397–405 (2014).
39. Kang, J. et al. A conformable microneedle sensor with photopatternable skin adhesive and gel electrolyte for continuous glucose monitoring. *Device* **1**, 100112 (2023).
40. Reynoso, M. et al. 3D-printed, aptamer-based microneedle sensor arrays using magnetic placement on live rats for pharmacokinetic measurements in interstitial fluid. *Biosens. Bioelectron.* **244**, 115802 (2024).
41. Yabut, J. M. et al. Emerging roles for serotonin in regulating metabolism: new implications for an ancient molecule. *Endocr. Rev.* **40**, 1092–1107 (2019).
42. Faraji Rad, Z., Prewett, P. D. & Davies, G. J. High-resolution two-photon polymerization: the most versatile technique for the fabrication of microneedle arrays. *Microsyst. Nanoeng.* **7**, 1–17 (2021).
43. Dervisevic, M., Harberts, J., Sánchez-Salcedo, R. & Voelcker, N. H. 3D Polymeric lattice microstructure-based microneedle array for transdermal electrochemical biosensing. *Adv. Mater.* **36**, 2412999 (2024).
44. Azarikhah, P. et al. A critical review of advances and challenges in microinjection moulding of polymeric microneedles. *J. Drug Deliv. Sci. Technol.* **114**, 107435 (2025).
45. Koelmans, W. et al. Microneedle characterization using a double-layer skin simulant. *Mech. Eng. Res.* **3**, p51 (2013).
46. Nakatsuka, N. et al. Aptamer–field-effect transistors overcome Debye length limitations for small-molecule sensing. *Science* **362**, 319–324 (2018).
47. Min, J. et al. Continuous biochemical profiling of the gastrointestinal tract using an integrated smart capsule. *Nat. Electron.* **8**, 844–855 (2025).
48. Ferguson, B. S. et al. Real-time, aptamer-based tracking of circulating therapeutic agents in living animals. *Sci. Transl. Med.* **5**, 213ra165 (2013).
49. Vaidya, R., Atanasov, P. & Wilkins, E. Effect of interference on the performance of glucose enzyme electrodes using Nafion® coatings. *Med. Eng. Phys.* **17**, 416–424 (1995).
50. Barradas, M. A., Gill, D. S., Fonseca, V. A., Mikhailidis, D. P. & Dandona, P. Intraplatelet serotonin in patients with diabetes mellitus and peripheral vascular disease. *Eur. J. Clin. Invest.* **18**, 399–404 (1988).
51. Young, R. L. et al. Augmented capacity for peripheral serotonin release in human obesity. *Int. J. Obes.* **42**, 1880–1889 (2018).
52. Malyszko, J., Urano, T., Takada, Y. & Takada, A. Stress-dependent changes in fibrinolysis, serotonin and platelet aggregation in rats. *Life Sci.* **54**, 1275–1280 (1994).
53. Takada, Y., Ihara, H., Urano, T. & Takada, A. Changes in blood and plasma serotonergic measurements in rats—effect of nicotine and/or exposure to different stresses. *Thromb. Res.* **80**, 307–316 (1995).
54. Teradaira, R. et al. Mental stress-induced changes in plasma serotonin, tryptophan, kynurenine concentrations in healthy participants. *Int. Congr. Ser.* **1304**, 175–179 (2007).
55. Lyte, J. M. et al. Gut–brain axis serotonergic responses to acute stress exposure are microbiome-dependent. *Neurogastroenterol. Motil.* **32**, e13881 (2020).
56. Van Cromphaut, S. J. Hyperglycaemia as part of the stress response: the underlying mechanisms. *Best Pract. Res. Clin. Anaesthesiol.* **23**, 375–386 (2009).
57. Rebrin, K. et al. Subcutaneous glucose monitoring by means of electrochemical sensors: fiction or reality? *J. Biomed. Eng.* **14**, 33 (1992).
58. Moatti-Sirat, D. et al. Towards continuous glucose monitoring: in vivo evaluation of a miniaturized glucose sensor implanted for several days in rat subcutaneous tissue. *Diabetologia* **35**, 224–230 (1992).
59. Wisniewski, N. & Reichert, M. Methods for reducing biosensor membrane biofouling. *Colloids Surf. B Biointerfaces* **18**, 197–219 (2000).
60. Leung, K. K., Downs, A. M., Ortega, G., Kurnik, M. & Plaxco, K. W. Elucidating the mechanisms underlying the signal drift of electrochemical aptamer-based sensors in whole blood. *ACS Sens.* **6**, 3340–3347 (2021).
61. Yamada, J., Sugimoto, Y., Kimura, I., Takeuchi, N. & Horisaka, K. Serotonin-induced hypoglycemia and increased serum insulin levels in mice. *Life Sci.* **45**, 1931–1936 (1989).

62. Sumara, G., Sumara, O., Kim, J. K. & Karsenty, G. Gut-derived serotonin is a multifunctional determinant to fasting adaptation. *Cell Metab.* **16**, 588–600 (2012).
63. Audhya, T., Adams, J. B. & Johansen, L. Correlation of serotonin levels in CSF, platelets, plasma, and urine. *Biochim. Biophys. Acta Gen. Subj.* **1820**, 1496–1501 (2012).
64. Levine, S. P. et al. Platelet activation and secretion associated with emotional stress. *Circulation* **71**, 1129–1134 (1985).
65. Sánchez, S. et al. Circadian variations of serotonin in plasma and different brain regions of rats. *Mol. Cell. Biochem.* **317**, 105–111 (2008).

Methods

Materials and reagents

PS ($M_W \approx 280{,}000$), Nafion 117, glucose oxidase (GOx), D-glucose (dextrose), 6-mercapto-1-hexanol, tris(hydroxymethyl)aminomethane hydrochloride (Tris–HCl), tris(2-carboxyethyl)phosphine hydrochloride (TCEP), ethylenediaminetetraacetic acid (EDTA) and anhydrous toluene were purchased from Sigma-Aldrich. Polyethylene terephthalate (PET) films were obtained from McMaster-Carr. PDMS (SYLGARD 184) was purchased from Dow Corning. Photocurable ultraviolet (UV) resin (Standard Resin) was obtained from ELEGOO. Tetrachloroauric(III) acid trihydrate ($HAuCl_4 3H_2O$) and iron(III) chloride ($FeCl_3$) were purchased from Thermo Fisher Scientific. Hydrochloric acid (HCl), acetic acid and phosphate-buffered saline (PBS) were obtained from Fisher Scientific. The 5-HT-sensing aptamer (5′-HS-CGACTGGTAGGCAGATAGGGGAAGCTGATTCGATGCGTGG GTCG-MB-3′)[46,47] was obtained from Integrated DNA Technologies. Serotonin creatinine sulfate monohydrate was obtained from Thermo Fisher Scientific. The 5-HT ELISA kit was purchased from DLD Diagnostika. Fetal bovine serum (FBS) was obtained from VWR. Medical tape (3M Tegaderm 1624W), a commercial glucometer (AUVON Blood Glucose Monitor Kit) and standard rat diet (PicoLab Rodent Diet 5053) were used for in vivo studies.

Fabrication of the microneedle array

The overall fabrication process is illustrated in Supplementary Fig. 7. A master needle array was generated via TPP 3D printing. This master was used to create a PDMS (10:1 ratio) mould, which was degassed and cured at 60 °C.

To form the structural microneedle plate, PS dissolved in toluene (40% w/v; viscosity, 500 cP; Supplementary Fig. 36) was utilized. For the ultrasound-assisted method, the PDMS mould was immersed in a glass vial containing the solution and left for 30 min to ensure solvent saturation. The entire vial was then subjected to a brief ultrasound treatment (1 min, 110 W at 40 kHz) to ensure complete filling of the cavities. For comparison, three alternative filling methods were employed: for the vacuum method, the solution was dropped onto the mould followed by vacuum treatment for 10 min; for the plasma method, the PDMS mould was treated with O_2 plasma (Plasma Etch PE-25, 100 W) for 10 min prior to casting the solution; and for the centrifugation method, the mould filled with the solution was spun at 3,005*g* (4,000 r.p.m.) for 5 min. All microneedle samples were dried at room temperature overnight and then baked at 50 °C on a hot plate for 2 h.

To create the flexible interface, a 75-µm-thick PET substrate was prepared with laser-cut via-holes and patterned electrode lines defined by masking tape. The resulting PS microneedle plate was then integrated onto the backside of the patterned PET substrate using a PS–toluene solution (1 g:10 ml ratio) as a structural adhesive.

Electrode metallization was performed via sequential sputtering. A Ti/Au (10 nm/500 nm) layer was first deposited on all electrodes, followed by an additional silver (300 nm) layer on the reference electrode and a Pt/Pt–Al (50 nm/120–160 nm) stack on the glucose-sensing and counter-electrodes. To define the active sensing area, the entire substrate was passivated by spin-coating a photocurable UV resin at 1,500 r.p.m. for 30 s twice. For the glucose sensor, a porous platinum surface was generated by selective dealloying of aluminium from the Pt–Al layer. A 7.5 µl droplet of 1 M $FeCl_3$ was dispensed onto each Pt–Al microneedle and allowed to react for 2 h in a sealed humid environment to minimize evaporation. The electrodes were then rinsed twice with deionized water and immersed in fresh deionized water for 2 h to remove residual etchant. The silver electrode was chlorinated with 1 M $FeCl_3$ for 3 min to yield a Ag/AgCl reference electrode.

Biosensor functionalization

5-HT sensor. The gold microneedle surface was first cleaned through cyclic voltammetry in 0.5 M NaOH (−1.6 to −1.0 V versus Ag/AgCl; scan rate, 1 V s^{-1}, 50 cycles) and 0.5 M H_2SO_4 (0.2–1.6 V versus Ag/AgCl; scan rate, 4 V s^{-1}, 100 cycles). A nanostructured gold layer was electrodeposited from 5 mM $HAuCl_4$ in 0.5 M HCl using pulse potentials of −0.4 V (1 s) and 0 V (1 s) for 180 cycles. For aptamer immobilization, a 100 µM aptamer stock in Tris–EDTA buffer was diluted to 10 µM, which was then reduced by mixing with 1 mM TCEP in a 1:1 volume ratio for 1 h in the dark. The reduced aptamer was diluted with PBS (pH 7.4) to 2.5 µM. Then 5 µl of the 2.5 µM aptamer solution was drop-cast onto the electrode and incubated for 2 h at room temperature in the dark. Unbound aptamers were rinsed with PBS (pH 7.4). The electrode was passivated with 5 mM 6-mercapto-1-hexanol in PBS (pH 7.4) overnight at 4 °C to cover the remaining electroactive surface.

Glucose sensor. The glucose sensor was fabricated on a dealloyed porous platinum microneedle surface. A mixture consisting of 10 mg ml^{-1} GOx in PBS (pH 7.4) and 1% (w/v) chitosan (in 2% w/v acetic acid) was prepared in a 1:2 volume ratio. Then 3 µl of the mixture was drop-cast onto the needle and dried for 2 h at room temperature. Subsequently, 3 µl of 1 wt% Nafion (diluted in a 1:4 mixture of H_2O and ethanol) was applied as an overcoat and dried overnight at 4 °C.

Characterization and measurements

Electrochemical characterization and measurements were performed using a CHI 1430 electrochemical workstation (CH Instruments), except for the wireless monitoring in freely moving animals. SWV was conducted within a potential range of −0.5 to 0 V (versus Ag/AgCl) with an increment of 5 mV and an amplitude of 20 mV. Amperometric measurements were performed at a constant potential of 0.55 V (versus Ag/AgCl). Calibration curves were established using three independently fabricated sensors ($n = 3$), with data points represented as mean ± s.d.

For signal quantification, the background current in SWV was removed by linear regression of the data points outside the redox peak region, typically excluding a ±0.1-V window centred at the peak potential. The resulting linear baseline was subtracted from the voltammogram to determine the net peak current. For continuous in vivo monitoring, the sensors were interrogated using a synchronized 120-s measurement cycle. Within each cycle, 5-HT sensing was executed first using SWV, followed by a 30-s amperometric measurement for glucose sensing. The current recorded at the end of the 30-s interval was extracted as the analytical signal. The remainder of the cycle was maintained as an electrical idle period to minimize continuous electrochemical load of the sensor interface.

During long-term in vivo testing, gradual baseline drift of the glucose sensor was corrected by subtracting a fitted linear baseline prior to concentration conversion (Supplementary Fig. 33). To convert these corrected electrochemical signals into real-time concentration profiles, a post-in vivo calibration protocol was performed at the conclusion of each animal experiment. With the sensor still stably in place, the animal was re-anaesthetized, and reference blood samples were collected every 10 min. A linear regression was then established using six calibration data points for each sensor: the KDM signal was fitted against the log-transformed serum 5-HT concentration (quantified via ELISA), and the baseline-corrected amperometric current was fitted against the blood glucose concentration (quantified via glucometer). These sensor-specific calibration relationships were subsequently applied to the continuous electrochemical recordings to generate dynamic concentration profiles.

Microneedle structure and surface morphology were characterized by SEM (Zeiss 1550VP FESEM). Microneedle insertion force–distance profiles were measured using a Mark-10 ESM303 tensile tester. To evaluate contact stability, impedance–time traces were acquired using a CHI 760E electrochemical workstation (CH Instruments). Measurements were performed in a two-electrode configuration between the electrodeposited gold microneedle (identical to the 5-HT sensing microneedle) and the porous platinum microneedle (identical to the counter microneedle) of the same microneedle array. The following

parameters were applied: initial potential, 0 V; a.c. perturbation amplitude, 0.1 V; frequency, 100 Hz; sample interval, 1 s.

Animal studies

All animal procedures were performed in accordance with protocols approved by the California Institute of Technology Institutional Animal Care and Use Committee (protocol number IA23-1800). Male Sprague–Dawley rats (300–400 g, 11–13 weeks old, Crl:CD(SD), Charles River Laboratories) were housed under standard conditions with a 13/11-h light/dark cycle (lights on at 06:00). For the rat studies, 20 animals were tested (one contact stability test across different postures, one contact stability test for cyclic motion, two long-term contact stability tests in freely moving rats, two postinsertion sensitivity tests, two injection tests, three in vivo sensor stabilization tests, three stress tests, three feeding tests and three unrestricted behaviour tests). Animals were provided with water and an irradiated rodent diet (PicoLab Rodent Diet 5053, PMI Nutrition International) ad libitum. Prior to all experiments, microneedle sensors were applied to the shaved and sterilized (70% ethanol) dorsal skin under isoflurane anaesthesia (5% induction, 1.5–2.5% maintenance via nose cone).

In vivo contact stability assessment. Microneedle sensor arrays were secured using medical tape, with or without a microneedle holder depending on the experimental group. Following recovery from anaesthesia, animals moved freely in their home cages for 12 h. To evaluate interface stability, impedance–time traces were continuously recorded at 100 Hz between the gold-coated microneedle (5-HT electrode) and the porous platinum microneedle (counter-electrode).

5-HT injection. Under isoflurane anaesthesia, 0.5 mg kg^{-1} of serotonin creatinine sulfate monohydrate (in saline) was administered via the tail vein. Blood samples were collected every 20 min from the tail and saphenous veins to provide reference levels of 5-HT (ELISA) and glucose (glucometer), respectively.

Tapping-induced stress response. Rats were placed in a test cage until a stable physiological baseline was established. Acute stress was induced by manually tapping the cage at random intervals (0–2 taps s^{-1}) for 10 min. Following the stress event and the monitoring session, blood was collected every 10 min for 60 min from the tail and saphenous veins for post-in vivo sensor validation and calibration under isoflurane anaesthesia.

Feeding response monitoring. Rats were fasted for 24 h prior to the feeding event. After establishing a stable baseline, a single pellet of standard diet (PicoLab Rodent Diet 5053) was provided. Upon completion of the feeding event and the monitoring session, blood was collected every 10 min for 60 min from the tail and saphenous veins for post-in vivo sensor validation and calibration under isoflurane anaesthesia.

Diurnal variation monitoring. Sensor-equipped rats were monitored during unrestricted activity with free access to standard pellets. Following the monitoring period, blood was collected every 10 min for 60 min from the tail and saphenous veins for post-in vivo sensor validation and calibration under isoflurane anaesthesia.

FEA

Mechanical simulations were performed using Code_Aster 14.6 within Salome-meca 2020 to evaluate the strain-isolating performance of the microneedle biointerface. The tissue was modelled as a trilayered linear elastic structure (30 mm total thickness) comprising the stratum corneum (20 µm, Young's modulus, E = 100 MPa, Poisson's ratio, ν = 0.4), viable epidermis (100 µm, E = 5 MPa, ν = 0.499) and a bulk dermal layer (29.88 mm, E = 10 kPa, ν = 0.499). This substantial dermal thickness was adopted to approximate a semi-infinite medium, effectively eliminating boundary effects from underlying rigid tissues (for example, muscle or bone) and thereby focusing on the mechanical interactions at the skin–microneedle interface. Corresponding properties were assigned to the microneedle holder (E = 1 GPa, ν = 0.4), PS microneedles (E = 2 GPa, ν = 0.4), and medical adhesive tape (E = 10 MPa, ν = 0.499).

Statistics and reproducibility

No statistical methods were used to predetermine sample sizes but our sample sizes are similar to those reported in previous publications[26,29,47]. No animals or data points were excluded from the analyses. The experiments were not randomized. Physiological responses were monitored within individual animals relative to their own baseline, and results are presented as individual traces; therefore, animals were not assigned to separate experimental groups, and randomization was not applicable to this study design. Data collection and analysis were not performed blind to the conditions of the experiments. Data distribution was assumed to be normal but this was not formally tested. Statistical values are presented as mean ± s.d., and sample sizes (n) for all quantitative data are defined in the corresponding figure legends.

The ultrasound-assisted moulding behaviour shown in Fig. 2d was independently repeated three times with similar results. The penetration experiments shown in Fig. 2j,k were independently repeated three times with similar results. For the H&E-stained cross-section shown in Fig. 4i, similar insertion behaviour was observed in three separate sections after 24 h of application.

Reporting summary

Further information on research design is available in the Nature Portfolio Reporting Summary linked to this article.

Data availability

All data are available in the main text or the Supplementary Information. Source data for the main and Extended Data figures are provided with this paper.

Acknowledgements

We gratefully acknowledge the critical support and infrastructure provided for this work by the Kavli Nanoscience Institute at Caltech.

Author contributions

G.K. and W.G. initiated the concept and designed the studies. G.K., S.C., H.A., C.W., H.H., X.M., M.-J.K., J.Q. and J.M. performed device preparation, characterization, validation and sample analysis. G.K. and W.G. co-wrote the paper. All authors contributed to the data analysis and provided feedback on the paper.

Funding

This project was supported by National Institutes of Health grants R01DC021461 and R01HL155815, Army Research Office grant W911NF-23-1-0041, National Science Foundation grants 2145802 and 2444815, US Army Medical Research Acquisition Activity grant HT9425-24-1-0249, Advanced Research Projects Agency for Health Sprint for Women's Health award number ARPA-H-ICHUB-24-101-504 and the Heritage Medical Research Institute. G.K. was partially supported by Basic Science Research Program through the National Research Foundation of Korea (NRF) funded by the Ministry of Education (RS-2024-00406237) and by the Korea Health Industry Development Institute (KHIDI) (grant number HI19C1344).

Competing interests

The authors declare no competing interests.

Additional information

Extended data is available for this paper at https://doi.org/10.1038/s41565-026-02247-5.

Supplementary information The online version contains supplementary material available at https://doi.org/10.1038/s41565-026-02247-5.

Correspondence and requests for materials should be addressed to Wei Gao.

Peer review information *Nature Nanotechnology* thanks Hnin Yin Yin Nyein, Marc Parrilla, and the other, anonymous, reviewer(s) for their contribution to the peer review of this work.

https://doi.org/10.1038/s41565-026-02247-5

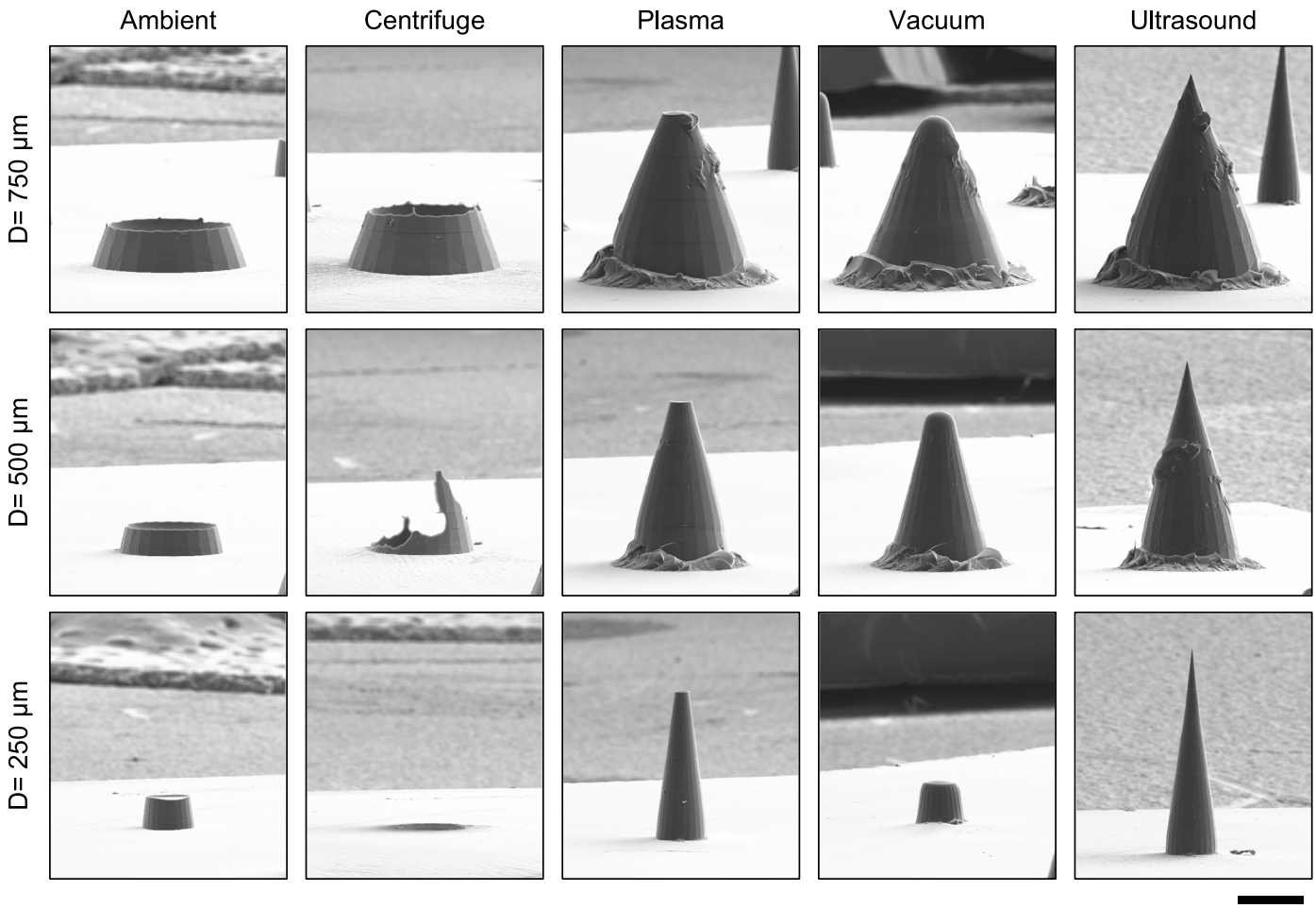

Extended Data Fig. 1 | Replication fidelity of microneedles fabricated using different moulding methods. SEM images of microneedles fabricated by ambient pressure, centrifugation, plasma treatment, vacuum, and ultrasound-assisted moulding (columns). Rows correspond to microneedles with varying base diameters (D = 750, 500, and 250 µm). Scale bar, 300 µm.

https://doi.org/10.1038/s41565-026-02247-5

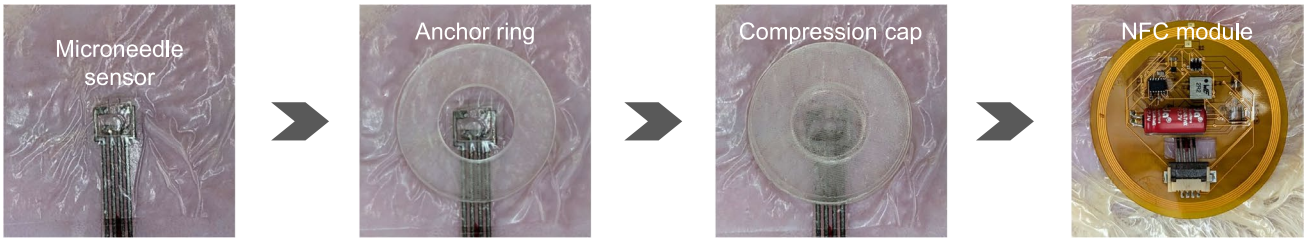

1. Attach the microneedle sensor using medical tape
2. Attach the anchor ring using double-sided tape.
3. Attach the compression cap using double-sided tape.
4. Connect the microneedle sensor to the NFC module.

Extended Data Fig. 2 | Assembly workflow for the strain-isolated wearable interface. Sequential photographs showing step-by-step integration of the microneedle sensor with the strain-isolating components (anchor ring and compression cap) and the wireless NFC module.

https://doi.org/10.1038/s41565-026-02247-5

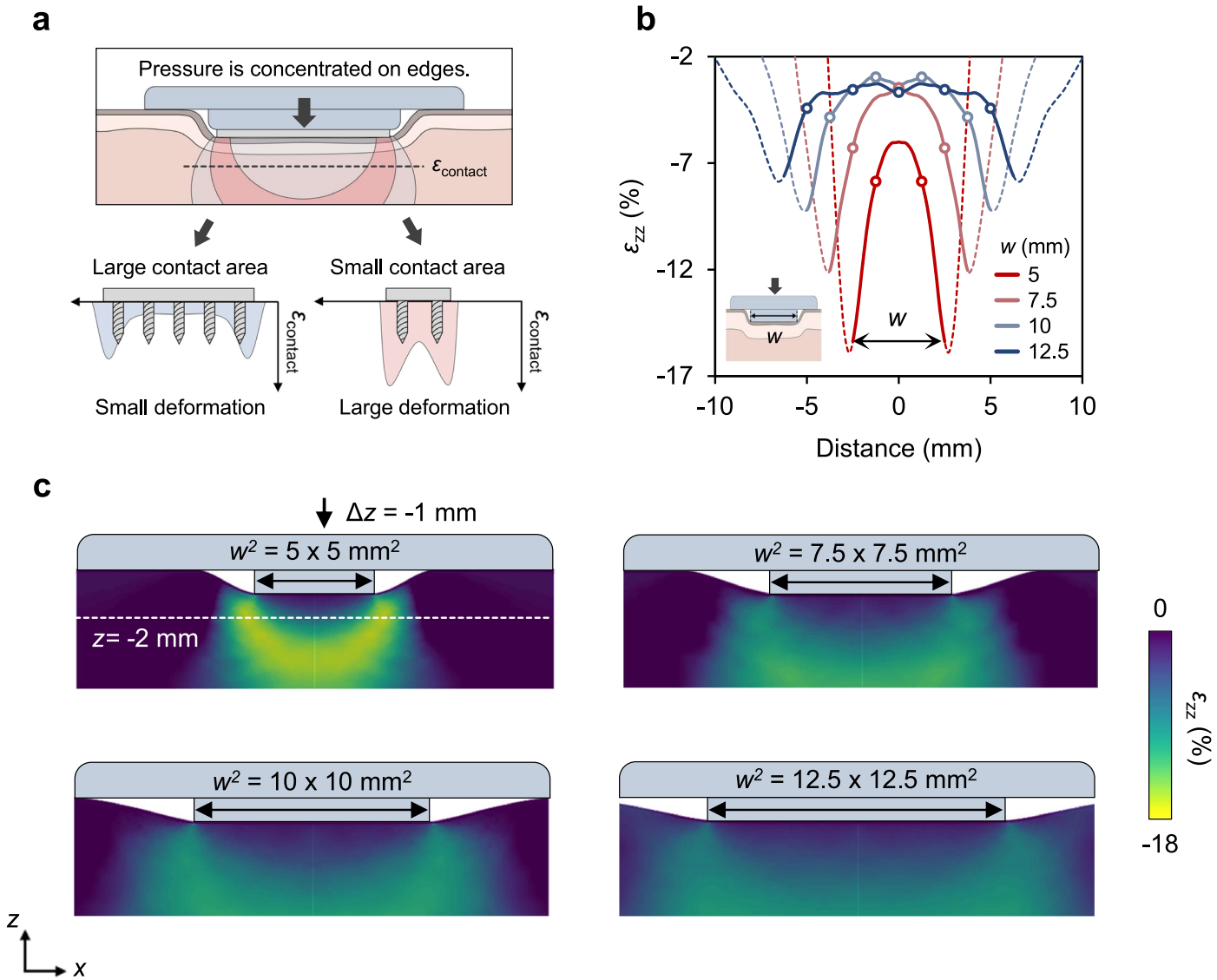

Extended Data Fig. 3 | Effect of compression area on vertical strain distribution for insertion stability. a, Mechanical design principle illustrating how reducing microneedle density concentrates compressive stress near the edges of the contact area, enhancing insertion stability. **b**, FEA results showing vertical strain (ε_{zz}) at a depth of 1 mm beneath the skin surface for compression caps of varying widths (w = 5–12.5 mm). White circles indicate microneedle positions corresponding to array sizes from 2×2 to 5×5. **c**, Cross-sectional maps showing the vertical strain (ε_{zz}) distribution in the skin induced by compression caps with varying contact areas (w^2 = 5 × 5 to 12.5 × 12.5 mm^2) at a fixed displacement (Δz = -1 mm). The white dashed line at z = -2 mm indicates the depth (1 mm below the compressed surface) where the strain profiles in **b** were extracted.

https://doi.org/10.1038/s41565-026-02247-5

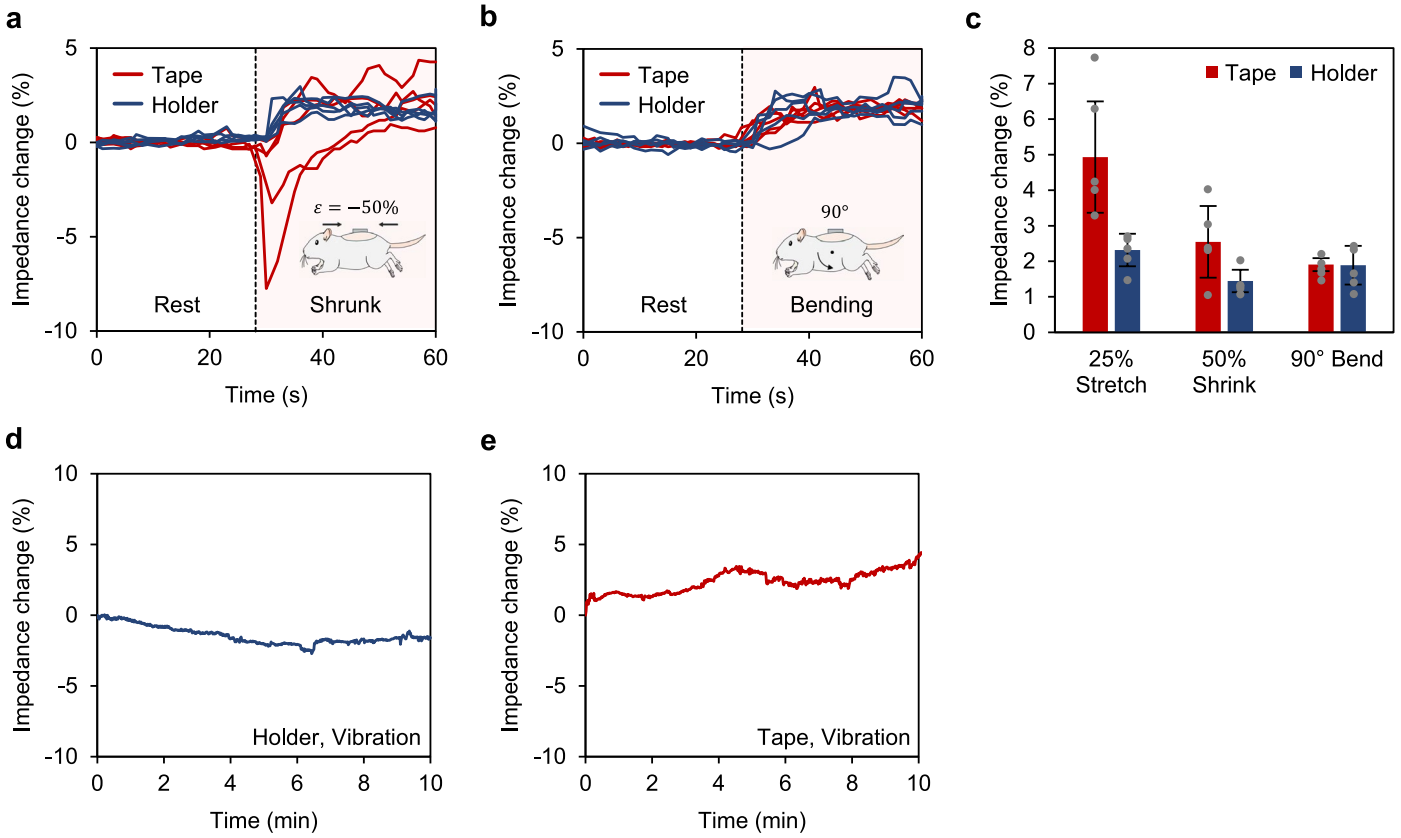

Extended Data Fig. 4 | Contact stability of microneedle sensors under skin deformation and vibration. a,**b**, Continuous impedance monitoring (at 100 Hz) of microneedle sensors secured with the strain-isolating holder (blue) versus medical tape (red) on a live rat during longitudinal skin compression (ε = −50%) (**a**) and static 90° bending (**b**). **c**, Summary of relative impedance changes under tensile (ε = 25%), compressive (ε = −50%), and 90° bending strains on live rats (n = 5). Bars represent mean ± s.d. **d**,**e**, Impedance variations of microneedles secured using the strain-isolating holder (**d**) or medical tape (**e**) during continuous vibration testing (1,000 r.p.m. for 10 min) on freshly euthanized rat skin.

https://doi.org/10.1038/s41565-026-02247-5

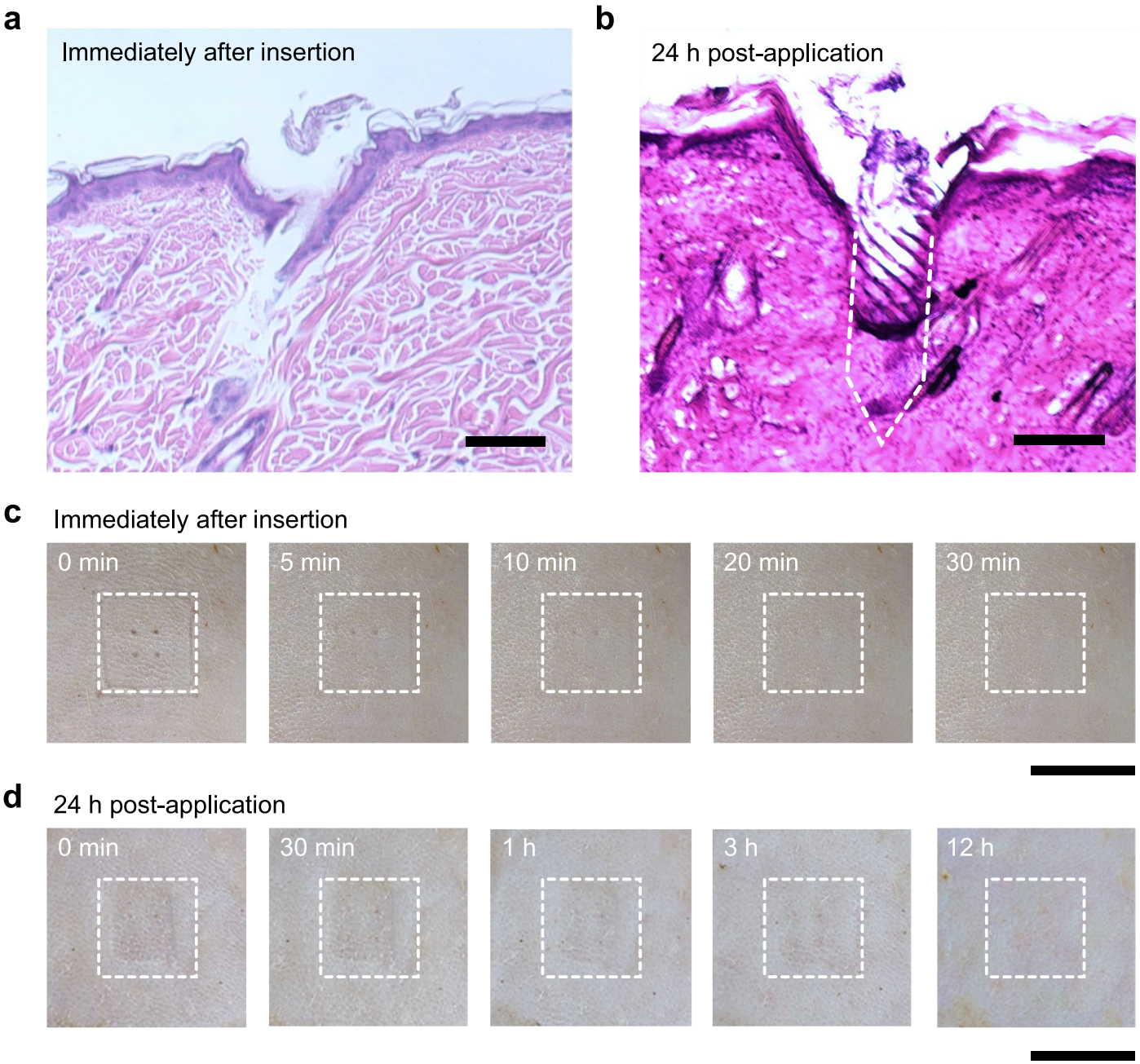

Extended Data Fig. 5 | Histological and macroscopic evaluation of microneedle insertion after prolonged ambulatory application. a, Representative haematoxylin and eosin (H&E)–stained cross-sectional image of rat skin immediately after microneedle insertion. **b**, H&E-stained cross-sectional image of the skin 24 h after device application, showing the microneedle (white dashed outline) still embedded in the dermis. **c**, Time-lapse optical images of the skin insertion site (white dashed boxes) taken at 0, 5, 10, 20, and 30 min after immediate microneedle removal. **d**, Time-lapse optical images of the skin insertion site at 0 min, 30 min, 1 h, 3 h, and 12 h after microneedle removal following 24 h of device application. Scale bars: 50 µm (**a**), 200 µm (**b**), and 1 cm (**c**, **d**).

https://doi.org/10.1038/s41565-026-02247-5

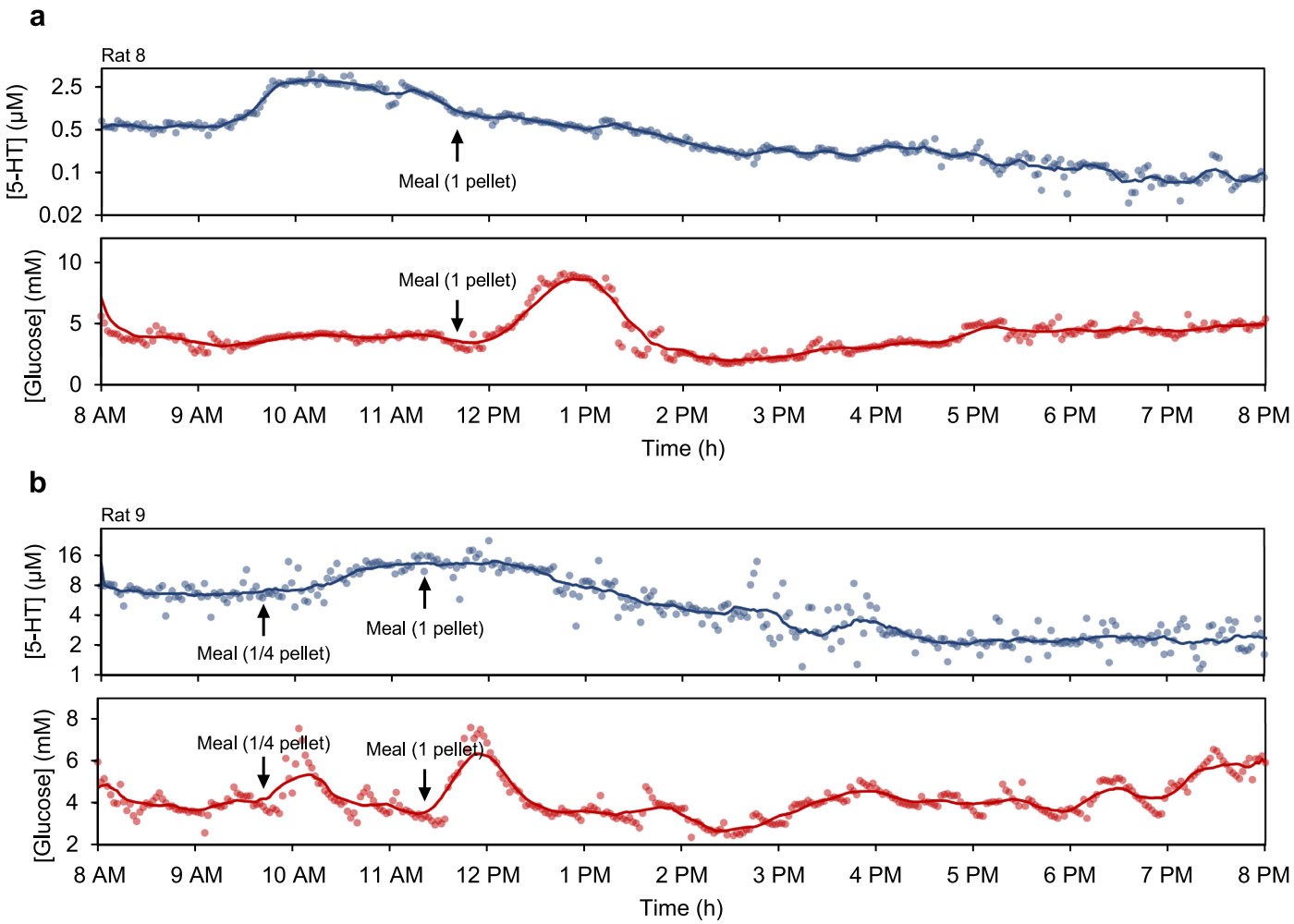

Extended Data Fig. 6 | Additional 12-h diurnal monitoring experiments. a,**b**, Continuous wireless monitoring of interstitial 5-HT and glucose levels in two additional freely moving animals over a 12-h diurnal cycle. Arrows indicate feeding events.

nature portfolio

Corresponding author(s): Wei Gao

Last updated by author(s): Jul 5, 2026

Reporting Summary

Nature Portfolio wishes to improve the reproducibility of the work that we publish. This form provides structure for consistency and transparency in reporting. For further information on Nature Portfolio policies, see our Editorial Policies and the Editorial Policy Checklist.

Statistics

For all statistical analyses, confirm that the following items are present in the figure legend, table legend, main text, or Methods section.

n/a	Confirmed
☐	☒ The exact sample size (*n*) for each experimental group/condition, given as a discrete number and unit of measurement
☐	☒ A statement on whether measurements were taken from distinct samples or whether the same sample was measured repeatedly
☒	☐ The statistical test(s) used AND whether they are one- or two-sided *Only common tests should be described solely by name; describe more complex techniques in the Methods section.*
☒	☐ A description of all covariates tested
☒	☐ A description of any assumptions or corrections, such as tests of normality and adjustment for multiple comparisons
☐	☒ A full description of the statistical parameters including central tendency (e.g. means) or other basic estimates (e.g. regression coefficient) AND variation (e.g. standard deviation) or associated estimates of uncertainty (e.g. confidence intervals)
☒	☐ For null hypothesis testing, the test statistic (e.g. *F*, *t*, *r*) with confidence intervals, effect sizes, degrees of freedom and *P* value noted *Give P values as exact values whenever suitable.*
☒	☐ For Bayesian analysis, information on the choice of priors and Markov chain Monte Carlo settings
☒	☐ For hierarchical and complex designs, identification of the appropriate level for tests and full reporting of outcomes
☒	☐ Estimates of effect sizes (e.g. Cohen's *d*, Pearson's *r*), indicating how they were calculated

Our web collection on statistics for biologists contains articles on many of the points above.

Software and code

Policy information about availability of computer code

Data collection	CH Instruments electrochemical analyzer (potentiostat) was used for sensor characterization and data collection. FEIG ISOStart v11.12.00 was used for NFC operation.
Data analysis	Microsoft Excel and MATLAB R2022a (MathWorks) were used to analyze and plot the data. Finite element simulations were performed using Code_Aster 14.6 within the Salome-Meca 2020 platform.

For manuscripts utilizing custom algorithms or software that are central to the research but not yet described in published literature, software must be made available to editors and reviewers. We strongly encourage code deposition in a community repository (e.g. GitHub). See the Nature Portfolio guidelines for submitting code & software for further information.

Data

Policy information about availability of data

All manuscripts must include a data availability statement. This statement should provide the following information, where applicable:

- Accession codes, unique identifiers, or web links for publicly available datasets
- A description of any restrictions on data availability
- For clinical datasets or third party data, please ensure that the statement adheres to our policy

All data supporting the findings of this study are available within the paper and its Supplementary Information. Source data are provided with this paper.

Research involving human participants, their data, or biological material

Policy information about studies with human participants or human data. See also policy information about sex, gender (identity/presentation), and sexual orientation and race, ethnicity and racism.

Reporting on sex and gender	n/a
Reporting on race, ethnicity, or other socially relevant groupings	n/a
Population characteristics	n/a
Recruitment	n/a
Ethics oversight	n/a

Note that full information on the approval of the study protocol must also be provided in the manuscript.

Field-specific reporting

Please select the one below that is the best fit for your research. If you are not sure, read the appropriate sections before making your selection.

☒ Life sciences ☐ Behavioural & social sciences ☐ Ecological, evolutionary & environmental sciences

For a reference copy of the document with all sections, see nature.com/documents/nr-reporting-summary-flat.pdf

Life sciences study design

All studies must disclose on these points even when the disclosure is negative.

Sample size	No statistical methods were used to pre-determine sample sizes; sample sizes are similar to those in previous publications on wearable in vivo biosensors and were sufficient to observe consistent trends. For material and sensor characterization, n = 3 independently prepared samples were used. For the rat studies, 20 animals were tested (1 contact stability test across different postures, 1 contact stability test for cyclic motion, 2 long-term contact stability tests in freely moving rats, 2 post-insertion sensitivity tests, 2 injection tests, 3 in vivo sensor stabilization tests, 3 stress tests, 3 feeding tests, and 3 unrestricted behavior tests).
Data exclusions	No animals or data points were excluded from the analyses.
Replication	Reproducibility was verified across all major experiments. Material and sensor characterizations were performed using at least three independently prepared samples (n = 3) with consistent results. Representative micrographs were independently repeated three times with similar results. All in vivo experiments were replicated using independent animals, and consistent physiological dynamics were observed across all tested animals for stress, feeding, and diurnal monitoring studies.
Randomization	Randomization was not relevant to this study. Physiological responses were monitored within individual animals relative to their own baseline and presented as individual traces; therefore, animals were not assigned to separate experimental groups, and randomization was not applicable.
Blinding	Data collection and analysis were not performed blind to the conditions of the experiments, as the study focuses on device validation with measurements interpreted against objective reference standards.

Reporting for specific materials, systems and methods

We require information from authors about some types of materials, experimental systems and methods used in many studies. Here, indicate whether each material, system or method listed is relevant to your study. If you are not sure if a list item applies to your research, read the appropriate section before selecting a response.

Materials & experimental systems

n/a	Involved in the study
☒	☐ Antibodies
☒	☐ Eukaryotic cell lines
☒	☐ Palaeontology and archaeology
☐	☒ Animals and other organisms
☒	☐ Clinical data
☒	☐ Dual use research of concern
☒	☐ Plants

Methods

n/a	Involved in the study
☒	☐ ChIP-seq
☒	☐ Flow cytometry
☒	☐ MRI-based neuroimaging

Animals and other research organisms

Policy information about studies involving animals; ARRIVE guidelines recommended for reporting animal research, and Sex and Gender in Research

Laboratory animals	Male Sprague–Dawley rats [Crl:CD(SD); Charles River Laboratories, Wilmington, MA, USA], 11–13 weeks old, 300–400 g, were used. As these are outbred wild-type animals, no specific genetic background modification applies. A total of 20 animals were used across all experiments (1 contact stability test across different postures, 1 contact stability test for cyclic motion, 2 long-term contact stability tests in freely moving rats, 2 post-insertion sensitivity tests, 2 injection tests, 3 in vivo sensor stabilization tests, 3 stress tests, 3 feeding tests, and 3 unrestricted behavior tests).
Wild animals	n/a
Reporting on sex	Male rats were used for all experiments. Sex-based analysis was not performed as this study focuses on device validation and proof-of-concept sensing performance rather than sex-dependent physiological differences.
Field-collected samples	n/a
Ethics oversight	The animal study protocol was approved by the Institutional Animal Care and Use Committee (IACUC) at the California Institute of Technology (protocol no. IA23-1800).

Note that full information on the approval of the study protocol must also be provided in the manuscript.

Plants

Seed stocks	n/a
Novel plant genotypes	n/a
Authentication	n/a